**International Journal of Fracture manuscript No.**
(will be inserted by the editor)

# Cavitation in Rubber: An Elastic Instability or a Fracture Phenomenon?

**Victor Lefèvre · K. Ravi-Chandar · Oscar Lopez-Pamies**

Received: date / Accepted: date

**Abstract** The viewpoint that cavitation in rubber — that is, the sudden growth of inherent defects in rubber into large enclosed cavities in response to external stimuli — is a purely elastic phenomenon has long been known to be fundamentally incomplete. Essentially, this is because the local stretches around the defects at which cavitation initiates far exceed the elastic limit of the rubber, which therefore ought to inelastically deform by fracturing to accommodate their growth. Yet, rather remarkably, the classical heuristic *elastic* criterion stating that cavitation occurs at material points wherein the hydrostatic component of the stress reaches the critical value $P = 5/2\mu$, with $\mu$ denoting the initial shear modulus of the rubber, has been shown to agree reasonably well with a number of experimental observations. This agreement suggests that the elastic properties of rubber may play a significant — possibly even dominant — role on the occurrence of cavitation.

The purpose of this paper is to provide insight into the relevance of the elastic properties of rubber on the phenomenon of cavitation. To this end, the comprehensive *elastic* cavitation theory recently put forward by Lopez-Pamies et al. (2011a) is directly confronted to two classical sets of experiments that to date have been understood only in part: (*i*) the poker-chip experiments of Gent and Lindley (1959) and (*ii*) the experiments of Gent and Park (1984) dealing with cavitation near reinforcing filler particles. Specifically, both sets of experiments are theoretically reproduced under the assumptions that the underlying rubber is Gaussian (for any arbitrarily large deformation) and that its inherent defects are vacuous and isotropically distributed. Results are presented for when and where cavitation occurs in the specimens as well as for the ensuing growth and interaction of the cavities once they have been "nucleated". It is found that the elastic theoretical results are in good agreement with many of the qualitative but few of the quantitative features of the experiments. The reasons behind this remarkable partial agreement and its practical implications are discussed.

**Keywords** Defects · Elastomers · Finite strain · Post-bifurcation

Victor Lefèvre
Department of Civil and Environmental Engineering, University of Illinois, Urbana–Champaign, IL 61801-2352, USA
E-mail: vlefevre@illinois.edu

K. Ravi-Chandar
Department of Aerospace and Engineering Mechanics, The University of Texas at Austin, TX 78712–1221, USA
E-mail: ravi@utexas.edu

Oscar Lopez-Pamies
Department of Civil and Environmental Engineering, University of Illinois, Urbana–Champaign, IL 61801-2352, USA
Tel.: +1 (217) 244-1242
E-mail: pamies@illinois.edu

## 1 Introduction

Under certain conditions, large enclosed cavities may suddenly "appear" in the interior of rubber. This phenomenon has come to be popularly known as cavitation. It corresponds, at heart, to nothing more than to the growth of defects inherent in rubber. Such defects can be of various natures (e.g., weak regions of the polymer network, actual holes, particles of dust) and of various geometries ranging from submicron to supramicron in length scale (Gent, 1991). Roughly speaking, when rubber is subjected to critically large mechanical (or possibly other type of) forces, these underlying defects may suddenly grow elastically up to the point at which the surrounding polymeric chains reach their maximum elongation. Beyond that point, the defects may continue to grow inelastically by a fracture process, i.e., by the irreversible creation of new surfaces.

As a first theoretical attempt to explain and describe cavitation in rubber, Gent and Lindley (1959) proposed to consider the initiation of cavitation as an *elastic instability*. In essence, they examined the elastostatics problem of a single vacuous spherical cavity of infinitesimal size (or defect) embedded at the center of a Gaussian (i.e., Neo-Hookean) rubber ball that is subjected to uniform hydrostatic pressure on its outer boundary. Under the *idealization* that rubber remains an elastic solid for arbitrarily large deformations — in other words, under the assumption that the defect can only grow elastically — they found that as the applied pressure approaches the critical value

$$P = \frac{5}{2}\mu, \tag{1}$$

where $\mu$ denotes the initial shear modulus of the rubber at zero strain, the size of the cavity suddenly becomes finite. Based on this result, Gent and Lindley (1959) postulated that cavitation ensues at any point in the interior of rubber at which the hydrostatic component of the stress reaches the critical value (1). In a later effort, Ball (1982) formalized and extended the result (1) to arbitrary incompressible isotropic nonlinear elastic solids (not just Neo-Hookean). This more general result reads as

$$P = \int_1^\infty \frac{1}{z^3-1}\,\frac{\mathrm{d}\phi}{\mathrm{d}z}\left(z^{-2}, z, z\right)\mathrm{d}z, \tag{2}$$

where $\phi = \phi(\lambda_1, \lambda_2, \lambda_3)$ stands for the stored-energy function of the solid in terms of the principal stretches $\lambda_1, \lambda_2, \lambda_3$. The unbounded upper limit of integration in (2) reveals that the onset of cavitation depends on the behavior of the rubber at *infinitely large* deformations. While mathematically profound, this, of course, is physically incongruous since rubber behaves approximately as an elastic solid up to a critical set of large but *finite* deformations, beyond which, much like any other solid, it ruptures. Based on this observation, one might expect that the result (1), or more generally (2), is not applicable to real rubber. Yet, the result (1) has been shown by Gent and co-workers (see Gent, 1991 and references therein) to agree reasonably well with a number of experimental observations. This agreement suggests that the elastic properties of rubber may play a significant — possibly even dominant — role on the onset of cavitation.

Motivated by the plausible prominence that the elastic properties of rubber may have on cavitation, Lopez-Pamies et al. (2011a) have recently developed a theory that permits to examine, now in full generality, the occurrence of cavitation as an elastic instability. In particular, generalizing the classical results referred to above, this new theory allows to rigorously consider onset of cavitation (*i*) under arbitrary loading conditions (not just hydrostatic loading), (*ii*) for general nonlinear elastic solids (not just incompressible and isotropic), and (*iii*) distributions of defects with general shapes (not just a single spherical defect). The objective of this paper is to confront this theory directly to experimental results in order to gain definite insight into the relevance of the elastic properties of rubber on the phenomenon of cavitation; comparisons of similar nature between the "hydrostatic" cavitation criterion of Gent and Lindley (1959) and experiments have been provided earlier by Stringfellow and Abeyaratne (1989).

The organization of the paper is as follows. Section 2 recalls the elastic cavitation theory of Lopez-Pamies et al. (2011a) for the practically relevant case when the underlying defects at which cavitation can initiate are vacuous and their spatial distribution is random and isotropic. The specialization of this result to the basic case when the rubber is Gaussian is spelled out in subsection 2.1.1. Section 3 compares this latter theoretical result with the poker-chip experiments of Gent and Lindley (1959). Section

4 further compares the theory with the experiments of Gent and Park (1984) dealing with cavitation near reinforcing filler particles. For both sets of comparisons, the theoretical results are first presented for the onset of cavitation and then for the subsequent growth and interaction of the cavities once they have been "nucleated". Section 5 records some concluding remarks.

## 2 The elastic cavitation theory of Lopez-Pamies et al. (2011)

Stimulated by experimental evidence (Gent, 1991) and the partial success of the classical theoretical results (1)–(2), Lopez-Pamies et al. (2011) considered the phenomenon of cavitation in rubber as the sudden *elastic growth* of its underlying defects in response to critically large applied external loads. The defects at which cavitation can initiate were modeled as nonlinear elastic cavities of zero volume, but of arbitrary shape otherwise, that are randomly distributed throughout the rubber. This point of view led to formulating the problem of cavitation as the homogenization problem of nonlinear elastic solids containing zero-volume cavities (Lopez-Pamies, 2009), which in turn led to the construction of a general — yet computationally tractable — rigorous criterion for the onset of cavitation.

### 2.1 The case of a random isotropic distribution of vacuous defects

The purpose of this work is to confront this new theory to a host of experiments where, due to the processing of the specimens, the spatial distribution of defects is expected to be *random* and *isotropic*. We shall further assume that the defects are *vacuous*. Granted these geometric and constitutive features for the defects, the onset-of-cavitation criterion of Lopez-Pamies et al. (2011) can be stated as follows:

*Inside a rubber whose nonlinear elastic response is characterized by the stored-energy function $W(\mathbf{F})$, cavitation can first occur at material points where the Cauchy stress $\mathbf{T}$ satisfies the condition*

$$\mathbf{T} = \frac{1}{\det \mathbf{F}} \mathbf{S}_\bigstar(\mathbf{F})\, \mathbf{F}^T \quad \textit{with} \quad \mathbf{F} \in \partial \mathcal{Z}\left[f_\bigstar(\mathbf{F})\right], \tag{3}$$

*where $\partial\mathcal{Z}[f_\bigstar(\mathbf{F})]$ denotes the boundary of the zero set of $f_\bigstar(\mathbf{F})$,*

$$f_\bigstar(\mathbf{F}) \doteq \lim_{f_0 \to 0+} f(\mathbf{F}, f_0) \qquad \textit{and} \qquad \mathbf{S}_\bigstar(\mathbf{F}) \doteq \lim_{f_0 \to 0+} \frac{\partial E}{\partial \mathbf{F}}(\mathbf{F}, f_0). \tag{4}$$

*Here, the scalar functions $E(\mathbf{F}, f_0)$ and $f(\mathbf{F}, f_0)$ are defined by the initial-value problems*

$$f_0 \frac{\partial E}{\partial f_0} - E - \frac{1}{4\pi} \int_{|\boldsymbol{\xi}|=1} \max_{\boldsymbol{\omega}} \left[ \boldsymbol{\omega} \cdot \frac{\partial E}{\partial \mathbf{F}}\, \boldsymbol{\xi} - W\left(\mathbf{F} + \boldsymbol{\omega} \otimes \boldsymbol{\xi}\right) \right] \mathrm{d}\boldsymbol{\xi} = 0 \qquad \textit{with} \qquad E(\mathbf{F}, 1) = 0 \tag{5}$$

*and*

$$f_0 \frac{\partial f}{\partial f_0} - f - \frac{f}{4\pi} \int_{|\boldsymbol{\xi}|=1} \boldsymbol{\omega} \cdot \mathbf{F}^{-T} \boldsymbol{\xi}\, \mathrm{d}\boldsymbol{\xi} - \frac{1}{4\pi} \int_{|\boldsymbol{\xi}|=1} \boldsymbol{\omega} \cdot \frac{\partial f}{\partial \mathbf{F}}\, \boldsymbol{\xi}\, \mathrm{d}\boldsymbol{\xi} = 0 \qquad \textit{with} \qquad f(\mathbf{F}, 1) = 1, \tag{6}$$

*where $\boldsymbol{\omega}$ in (6) denotes the maximizing vector $\boldsymbol{\omega}$ in (5).*

The function $E$ defined by the first-order nonlinear pde (5) corresponds to the total elastic energy (per unit undeformed volume) characterizing the homogenized constitutive response of a nonlinear elastic solid with stored-energy function $W$ containing a certain isotropic distribution of disconnected vacuous cavities of initial volume fraction $f_0$. The function $f$ defined by the first-order linear pde (6), on the other hand, characterizes the evolution of the volume fraction of the cavities along finite-deformation loading paths. The asymptotic behavior (4) of these functions — in the limit as $f_0 \to 0+$ when the underlying cavities become *point defects* — are the quantities that serve to identify the critical stresses (3) at which cavitation ensues.

*2.1.1 Onset of cavitation in Gaussian rubber*

In all of the comparisons with experiments that follow, we shall assume that the nonlinear elastic response of rubber is Gaussian (or Neo-Hookean) and thus characterized by the stored-energy function

$$W(\mathbf{F}) = \begin{cases} \frac{\mu}{2}[\mathbf{F}\cdot\mathbf{F} - 3] & \text{if } \det\mathbf{F} = 1 \\ +\infty & \text{otherwise} \end{cases}, \tag{7}$$

where, again, $\mu$ stands for the initial shear modulus of the specific rubber under investigation. For this type of behavior, the limiting functions (4) can be shown to be given by

$$f_\star(\mathbf{F}) = 1 - \frac{1}{\det\mathbf{F}} \qquad \text{and} \qquad \mathbf{S}_\star(\mathbf{F}) = \mu\mathbf{F} + \frac{\mu(1+2\det\mathbf{F})}{2(\det\mathbf{F})^{1/3}}\,\Phi(\mathbf{F})\,\mathbf{F}^{-T} + \frac{3\mu(\det\mathbf{F}-1)}{2(\det\mathbf{F})^{1/3}}\,\frac{\partial\Phi}{\partial\mathbf{F}}(\mathbf{F}), \tag{8}$$

where the function $\Phi$ is defined implicitly by a first-order nonlinear pde in two variables (see Section 3.1 and Appendix C in Lopez-Pamies et al., 2011b). It is such that $\Phi(\mathbf{QFK}) = \Phi(\mathbf{F})\ \forall\mathbf{Q},\mathbf{K} \in Orth^+$ and $0 < \Phi(\mathbf{F}) \leq 1$ with $\Phi(\mathbf{Q}) = 1\ \forall\mathbf{Q} \in Orth^+$ and $\Phi(\mathbf{F}) \to 0$ as $||\mathbf{F}|| \to 0, +\infty$. For all practical purposes, as discussed in Section 6 of Lopez-Pamies et al. (2011b), the function $\Phi$ may be approximated simply as being equal to its maximum value $\Phi(\mathbf{F}) = 1$. By making use of this approximation, it is not difficult to deduce that the cavitation criterion (3)–(6) reduces in this case to:

*Inside Gaussian rubber, cavitation can first occur at material points where the principal Cauchy stresses $t_i$ $(i = 1, 2, 3)$ satisfy the condition*

$$8t_1t_2t_3 - 12\mu(t_1t_2 + t_2t_3 + t_3t_1) + 18\mu^2(t_1 + t_2 + t_3) - 35\mu^3 = 0 \quad \textit{with} \quad t_i > \frac{3}{2}\mu. \tag{9}$$

The interested reader is referred to Lopez-Pamies et al. (2011b) for the derivation and thorough discussion of the criterion (9). Here, it is relevant to record for later reference that for states of purely dilatational stress when $t_1 = t_2 = t_3 = P$, the general criterion (9) reduces, rather remarkably[1], to the approximate "hydrostatic" criterion proposed by Gent and Lindley (1959):

$$\frac{1}{3}(t_1 + t_2 + t_3) - \frac{5}{2}\mu = 0. \tag{10}$$

For more complex states of stress with non-vanishing shear ($\tau_1 \doteq t_2 - t_1 \neq 0$ and/or $\tau_2 \doteq t_3 - t_1 \neq 0$), the general criterion (9) — as opposed to the hydrostatic criterion (10) — indicates that cavitation occurs at mean stress values $P = (t_1 + t_2 + t_3)/3 > 5/2\mu$. In other words, shear stresses stabilize the rubber in the sense that their presence postpones the onset of cavitation.

## 3 Comparison of the theory with the poker-chip experiments of Gent and Lindley (1959)

In a seminal contribution, Gent and Lindley (1959) reported a beautiful set of experiments where cavitation was induced within thin disks of rubber bonded to metal plates subjected to unixaxial tensile forces. Specifically, the test-pieces were made up of thin disks of (filled and unfilled) natural rubber bonded to circular metallic plates by means of cement during the vulcanization process. The rubber disks were $R = 1$ cm in initial radius and from $H = 0.056$ cm to $H = 0.980$ cm in initial thickness (hence their name "poker-chip" experiments). The load was applied quasistatically under displacement control by means of a tensometer, which provided measurements of the load $\mathtt{f}$ induced by a given applied displacement $h - H$. Gent and Lindley (1959) reported these raw measurements in terms of the "macroscopic" stress measure $\overline{\sigma} \doteq \mathtt{f}/(\pi R^2)$ and the "macroscopic" strain measure $\overline{\varepsilon} \doteq h/H - 1$. Figure 1 depicts a schematic of the geometry and deformation of the specimens with the various quantities of interest indicated.

[1] Again, equation (10), as derived by Gent and Lindley (1959), corresponds to the case of a single defect that is vacuous and spherical in shape. By contrast, the result (9) corresponds to a random isotropic distribution of vacuous defects (not just one, but a distribution of infinitely many) which are not necessarily spherical in shape. Section 5 of Lopez-Pamies et al. (2011a) elaborates further on such a remarkable connection between the cavitation criterion (3)–(6) and the results of Gent and Lindley (1959) and of Ball (1982).

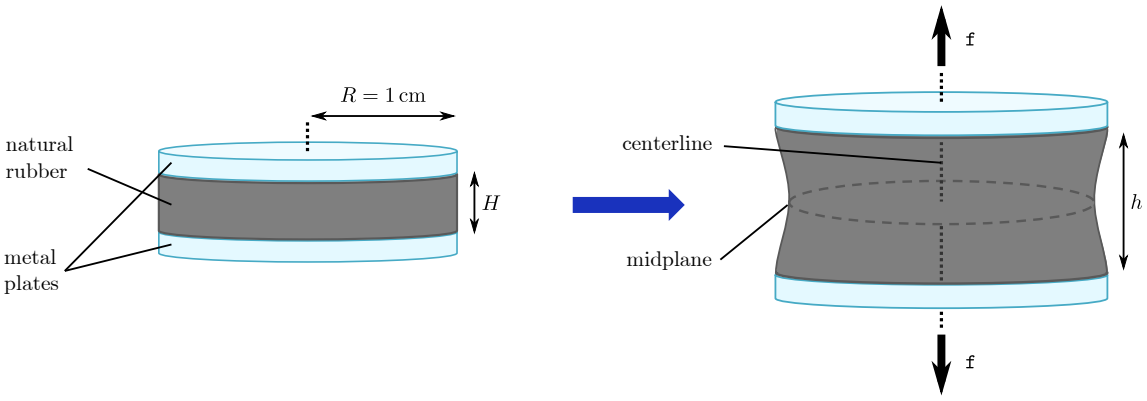


**Fig. 1** Schematic of the poker-chip experimental setup of Gent and Lindley (1959). The initial radius of the rubber disks was fixed at $R = 1$ cm, while their initial thicknesses were varied from $H = 0.056$ cm to $H = 0.980$ cm in order to induce stress fields with a wide range of triaxialities (from large for the thinnest disk to relatively small for the thickest one) inside the rubber.

In the sequel, we report finite-element (FE) simulations of the experiments of Gent and Lindley (1959). We begin in subsection 3.1 by showing when and where the cavitation criterion (9) is satisfied within three representative rubber disks: (*i*) the thinnest disk with $H = 0.056$ cm, (*ii*) the moderately thick disk with $H = 0.190$ cm, and (*iii*) the thickest disk with $H = 0.980$ cm, as a function of the applied macroscopic strain $\overline{\varepsilon}$. In subsection 3.2, we explicitly introduce defects — in the form of vacuous spherical cavities of $\Delta = 1$ $\mu$m radius — at the locations disclosed by the criterion into the FE models in order to investigate the ensuing growth and interaction of the "nucleated" cavities upon further loading. We dedicate subsection 3.3 to comparing the simulations with the experiments.

### 3.1 Pointwise monitoring of the cavitation criterion

*The FE model.* Due to the constitutive and geometric symmetries of the problem, it suffices to perform the calculations in just one half of a 2D-axisymmetric configuration of the rubber disk of interest; the metallic plates are assumed to be constitutively rigid and bonded perfectly to the rubber. The geometry of such regions is discretized via a uniform distribution of quadrilateral elements. Four-node hybrid linear elements with constant pressure are utilized in order to handle the incompressible behavior of the Gaussian rubber (7). Since the computations are carried out using the FE package ABAQUS, we make use of the CAX4H hybrid elements available in this code (see ABAQUS Version 6.11 Documentation). Mesh sensitivity studies reveal that structured meshes of this sort with a total number of elements in the order of 50,000 produce sufficiently accurate results for any of the geometries of interest here ($0.056\,\text{cm} \leq H \leq 0.980\,\text{cm}$).

*Results.* Figure 2 shows the deformed configurations of the rubber disk with thickness $H = 0.056$ cm at five values of the applied macroscopic strain, $\overline{\varepsilon} = 0, 0.2816, 0.2820, 0.2998$, and $1.40\%$. Material points at which the cavitation criterion (9) is satisfied are depicted in red. Incidentally, because of the extremely small thickness of the disk, they happen to also roughly coincide with the material points at which the hydrostatic cavitation criterion (10) is satisfied.

As indicated by arrows in Fig. 2(b), the first points to reach the cavitation criterion are those at the rubber/plates interfaces along the centerline of the disk. This is because — in contrast to popular belief in the literature — the hydrostatic stress in poker-chip experiments is always largest at the rubber/plates interfaces along the centerline of the test-piece, and *not* at the center of the rubber disk. As the applied strain $\overline{\varepsilon}$ increases, the region where the criterion is satisfied grows radially along the rubber/plates interfaces and also propagates to the center of the rubber disk reaching it at the value $\overline{\varepsilon} = 0.2820\%$; this is shown by Fig. 2(c). As the applied strain $\overline{\varepsilon}$ increases even further, the region where the criterion is satisfied continues to grow radially from the centerline of the disk towards its lateral free boundary. Figures 2(d) and (e) illustrate two snapshots of this propagation.

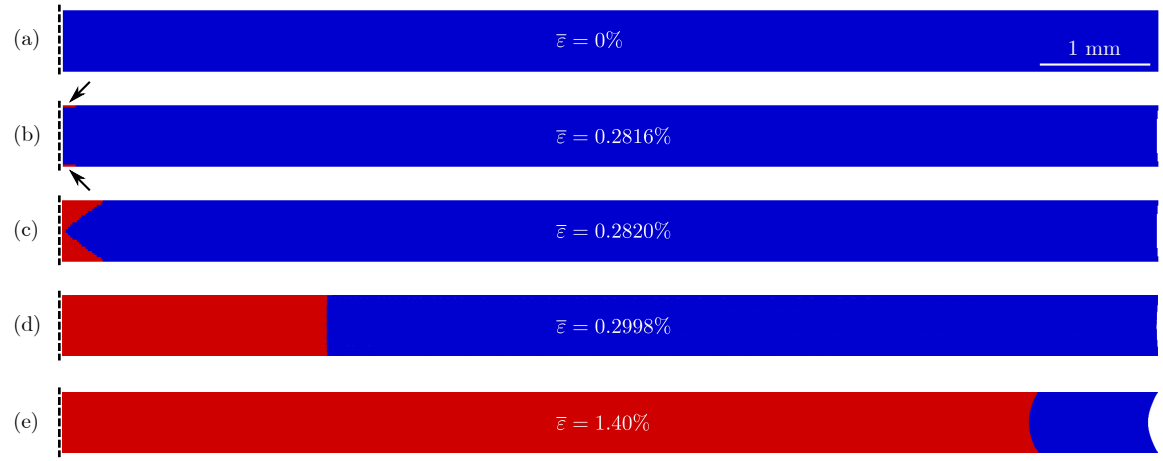


**Fig. 2** Axisymmetric FE simulation of the poker-chip experiment with rubber disk thickness $H = 0.056$ cm. Parts (a) through (e) show the deformed configurations of half (for better visualization) of the rubber disk at five values of the applied macroscopic strain $\overline{\varepsilon}$. The material points at which the cavitation criterion (9) is progressively satisfied are depicted in red.

Figure 3 shows the deformed configurations of the rubber disk with the larger thickness $H = 0.190$ cm at four values of the applied macroscopic strain, $\overline{\varepsilon} = 0, 3.119, 3.181$, and $5.30\%$. Material points at which the cavitation criterion (9) is satisfied are again depicted in red. For comparison purposes, the points at which the hydrostatic criterion (10) is satisfied are also depicted.

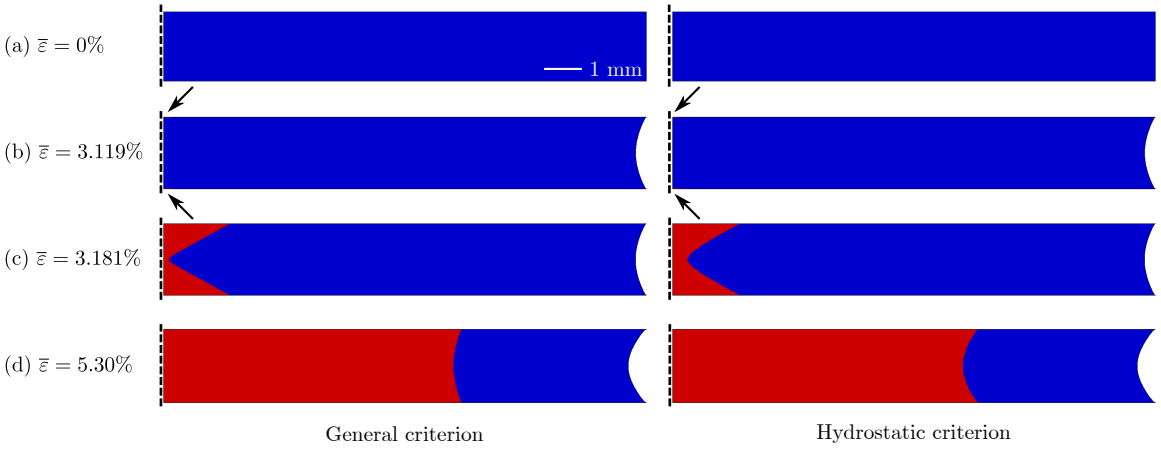


**Fig. 3** Axisymmetric FE simulation of the poker-chip experiment with rubber disk thickness $H = 0.190$ cm. Parts (a) through (d) show the deformed configurations of half (for better visualization) of the rubber disk at four values of the applied macroscopic strain $\overline{\varepsilon}$. The material points at which the general cavitation criterion (9) and the hydrostatic cavitation criterion (10) — included for comparison purposes — are progressively satisfied are depicted in red.

In qualitative agreement with the preceding simulations for the thinnest test-piece, Figs. 3(b) through (d) show that the first material points to satisfy the criterion (9) are those at the rubber/plates interfaces along the centerline of the disk. The region where the criterion is satisfied then grows radially along the rubber/plates interfaces and also to the center of the rubber disk. Ultimately, the region also grows radially towards the lateral boundary of the disk, albeit at a significantly slower rate than in the thinnest test-piece. Quantitatively, on the other hand, the results for this thicker rubber disk are quite different from those shown in Fig. 2. As illustrated by Fig. 3(b), the first occurrence of cavitation takes place at the much larger applied strain $\overline{\varepsilon} = 3.119\%$ (compared to $\overline{\varepsilon} = 0.2816\%$). This, of course, is expected since at equal values of the applied strain $\overline{\varepsilon}$ the hydrostatic stresses within the rubber decrease with increasing

disk thickness $H$. By the same token, the local values of the shear stresses $\tau_1 = t_2 - t_1$ and $\tau_2 = t_3 - t_1$ are much larger in the thicker disk and hence their influence on the onset of cavitation becomes noticeable. The influence of the shear stresses can be visualized by comparing the cavitation results based on the general criterion (9), shown in the left half of Fig. 3, with those based on the hydrostatic criterion (10), shown in the right half of the figure.

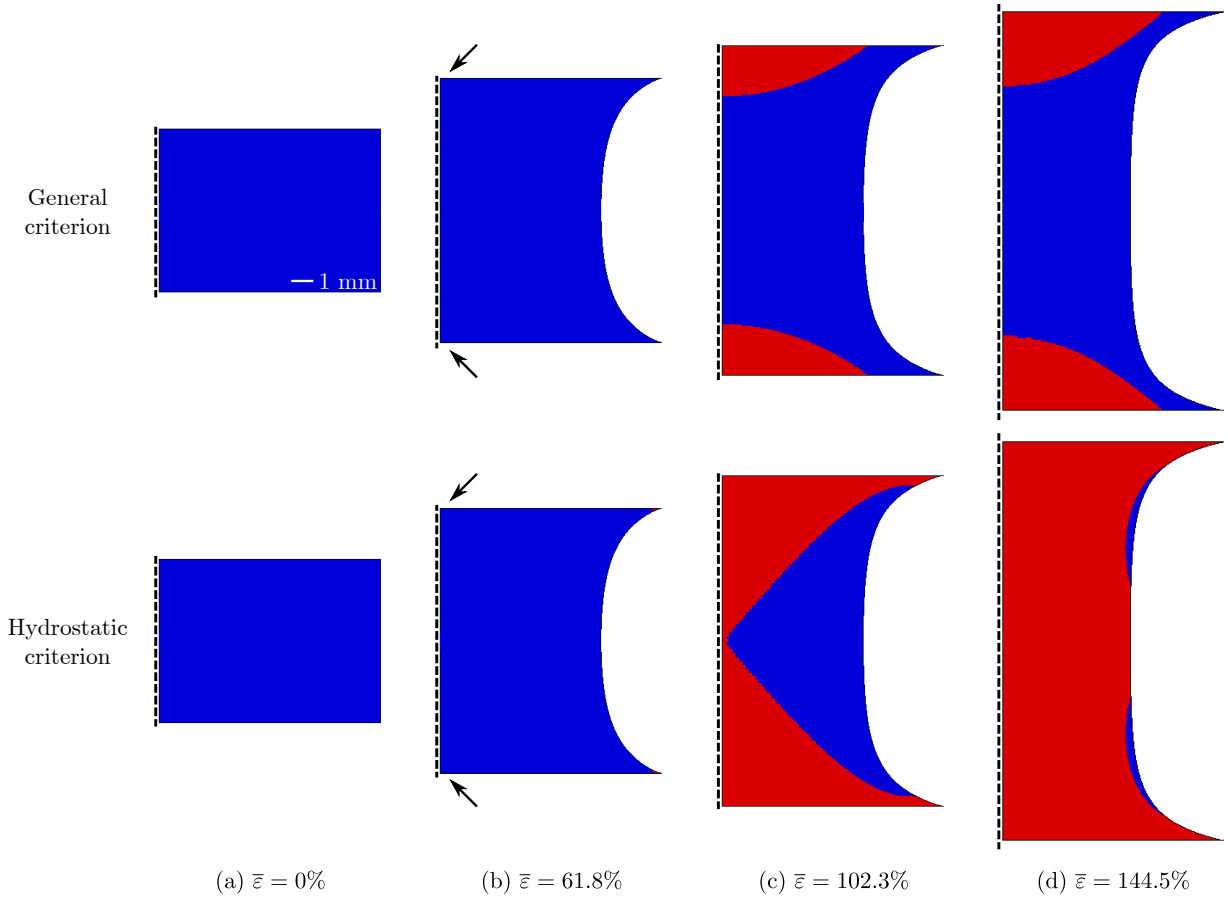


**Fig. 4** Axisymmetric FE simulation of the poker-chip experiment with rubber disk thickness $H = 0.980$ cm. Parts (a) through (d) show the deformed configurations of half (for better visualization) of the rubber disk at four values of the applied macroscopic strain $\overline{\varepsilon}$. The material points at which the general cavitation criterion (9) and the hydrostatic cavitation criterion (10) — included for comparison purposes — are progressively satisfied are depicted in red.

Finally, Fig. 4 shows the deformed configurations of the thickest rubber disk with $H = 0.980$ cm at the applied macroscopic strains $\overline{\varepsilon} = 0, 61.8, 102.3$, and $144.5\%$. The qualitative and quantitative trends pointed out above continue in the sense of when and where cavitation occurs as well as in that the local values of hydrostatic stress are smaller and those of shear stresses much larger than in the two previous cases with smaller $H$. Again, this latter point can be readily deduced by comparing the regions at which the general (9) and hydrostatic (10) criteria are satisfied. In particular, Figs. 4(c) and (d) show that the general criterion (9) remains unsatisfied away from the rubber/plates interfaces — never reaching the center of the disk in fact — irrespectively of the applied macroscopic strain. By contrast, the hydrostatic criterion (10) is satisfied almost everywhere for strains $\overline{\varepsilon} > 120\%$.

### 3.2 Full-field simulations accounting for the growth of the defects

The preceding analysis has served to reveal the critical macroscopic loads and associated spatial locations at which defects in rubber may start to grow to finite sizes during poker-chip experiments. In this subsection, we investigate the extent to which they grow and how they *interact* with one another. To this end, we introduce defects explicitly in the FE models at the locations disclosed by the criterion (9) and monitor their growth. Here, defects are modeled as vacuous spherical cavities of initial radius $\Delta = 1$ $\mu$m. In this regard, it is important to remark that we have performed a variety of simulations wherein the defects are micron and submicron in size and spherical and non-spherical in shape. Interestingly, the results of such simulations indicate that provided the defects are no larger than roughly 1 $\mu$m in length scale, their specific shape and size do not significantly influence when and how they grow (at least during the poker-chip simulations of interest here), hence our choice to model them as spherical cavities of initial radius $\Delta = 1$ $\mu$m.

#### *3.2.1 Defects along the centerline of the rubber disk*

Given that the attainability of the cavitation criterion (9) first occurs along the centerline of the rubber disk at its top and bottom faces and then — provided that the test-piece is sufficiently thin — propagates to its center, it is instructive to begin by considering the explicit presence of defects at those locations.

*The FE model.* Introducing spherical defects along the disk's centerline does not perturb the geometric symmetry of the problem and so — much like in the preceding analysis without defects — it suffices to carry out the calculations in one half of a 2D-axisymmetric configuration of the rubber disk of interest. As in the foregoing, four-node hybrid linear elements are utilized to discretize such regions with smaller elements placed around the defects. Figure 5 shows details of a representative structured mesh for the case when the defects are introduced at the top, bottom, and center of the disk: part (a) depicts the mesh near the top defect, while part (b) depicts the mesh near the defect at the center. Note that the defects at the top and bottom are positioned 1 $\mu$m away from the rubber/plates interfaces in order to be able to mesh them appropriately.

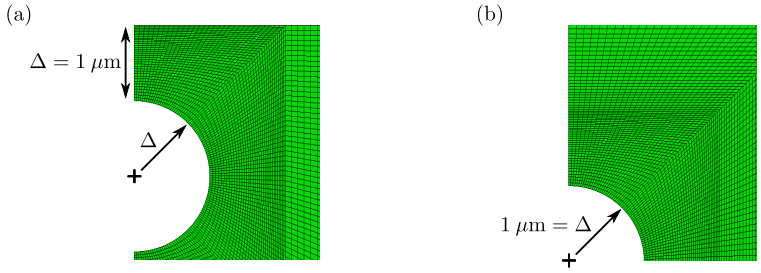


**Fig. 5** Details of the axisymmetric FE model for the poker-chip test-piece with rubber disk thickness $H = 0.056$ cm containing three defects along its centerline: two at the rubber/plates interfaces and one at its center. Part (a) shows the defect at the top rubber/plate interface, while part (b) shows the defect at the center of the rubber disk.

*Results.* Figure 6 shows results for the rubber disk with thickness $H = 0.056$ cm containing two and three defects. Parts (a)–(c) and (g) correspond to results for the case when two defects are located at the rubber/plates interfaces, whereas parts (d)–(f) and (h) correspond to the case when there is an additional third defect located at the center of the disk. In particular, Figs. 6(a)–(f) illustrate the deformed configurations of the rubber disk around its centerline at various values of the applied macroscopic strain $\overline{\varepsilon}$; the ratios $v^i/V$ and $v^c/V$ of current volumes $v^i$ and $v^c$ to initial volume $V = 4/3\pi\Delta^3 \approx 4.19 \times 10^{-18}\text{m}^3$ of the defects at the *i*nterfaces and *c*enter of the disk are also displayed in these figures to aid the visualization of their growth. To further aid the quantitative understanding, Figs. 6(g) and (h) present corresponding

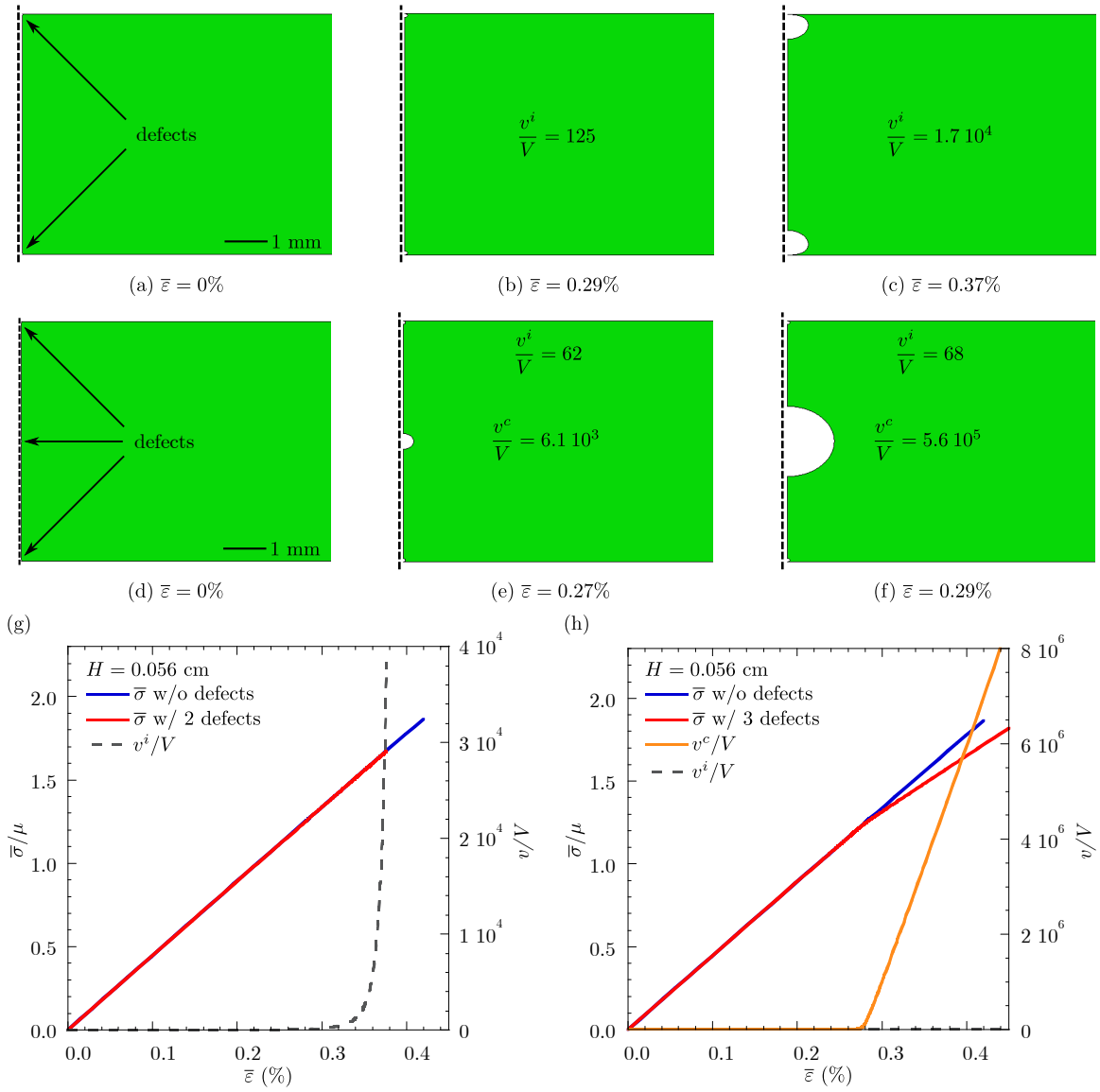


**Fig. 6** Axisymmetric FE simulations of the poker-chip experiment with rubber disk thickness $H = 0.056$ cm containing defects along the centerline of the disk. Parts (a) through (c) and (g) show results when two defects are located at the rubber/plates interfaces. On the other hand, parts (d) through (f) and (h) show results when there is an additional third defect located at the center. Figures (a)–(f) depict the deformed configurations of the rubber disk around its centerline at three values of the applied macroscopic strain $\overline{\varepsilon}$, while (g) and (h) show plots of the normalized macroscopic stress $\overline{\sigma}/\mu$ and volume variation $v/V$ of the defects as functions of $\overline{\varepsilon}$.

plots of the normalized macroscopic stress $\overline{\sigma}/\mu$ and volume variation $v/V$ of the defects as functions of the applied macroscopic strain $\overline{\varepsilon}$.

When the only defects that are accounted for are those at the rubber/plates interfaces, such defects start to grow to much larger sizes at around the critical strain $\overline{\varepsilon} = 0.2816\%$ predicted by the criterion (9). This is shown pictorially by Figs. 6(a)–(c) and quantitatively by Fig. 6(g). On the other hand, when an additional defect at the center of the disk is also accounted for, Figs. 6(d)–(f) and (h) show that all three defects start to grow at around the same strain ($\overline{\varepsilon} = 0.2816\%$), also as predicted by the criterion (9), but then the growth localizes in the defect at the center while those at the interfaces essentially stop growing. Such a strong interaction can be understood from the fact that the defects at the interfaces are

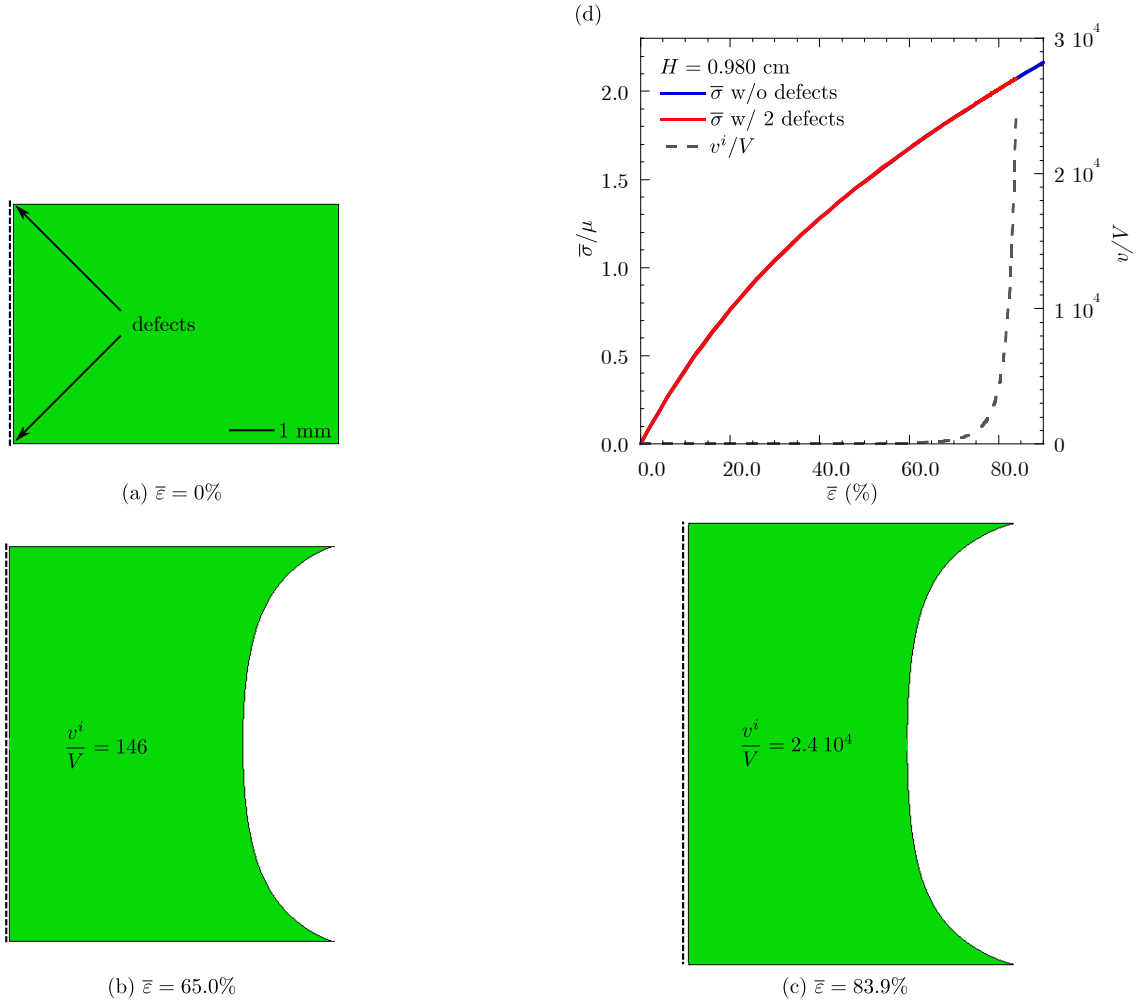


(a) $\overline{\varepsilon} = 0\%$

(b) $\overline{\varepsilon} = 65.0\%$

(c) $\overline{\varepsilon} = 83.9\%$

**Fig. 7** Axisymmetric FE simulation of the poker-chip experiment with rubber disk thickness $H = 0.980$ cm containing two defects located at the rubber/plates interfaces along the centerline of the disk. Parts (a), (b), and (c) depict the deformed configuration of half (for better visualization) of the rubber disk at three values of the applied macroscopic strain $\overline{\varepsilon}$. Part (d) shows plots of the normalized macroscopic stress $\overline{\sigma}/\mu$ and volume variation $v/V$ of the defects as functions of $\overline{\varepsilon}$.

comparatively more constrained to grow because of the rigidity of the nearby metal plates. Accordingly, it turns out to be energetically more favorable for the defect at the center to accommodate all of the growth.

The results in Fig. 6(h) also show that the macroscopic stress-strain relation for the rubber disk with three defects softens significantly — when compared to that of the perfect rubber disk without defects — right after the onset of cavitation. This is because of the geometric softening generated by the growth of the defect at the center. Interestingly, Fig. 6(g) shows that the same is *not* true for the rubber disk with defects only at the rubber/plates interfaces. This is consistent with the fact that the growth of defects near the rubber/plates interfaces is energetically costly.

The behavior of the rubber disk with thickness $H = 0.190$ cm containing analogous two and three defects along the centerline of the disk is essentially identical to that described in Fig. 6, and thus not reported here. On the other hand, as expected by the much larger values of shear stresses involved, the behavior of the disk with thickness $H = 0.980$ cm is quite different. This is shown by Fig. 7. Parts (a)–(c) of the figure depict the deformed configurations of the rubber disk at the applied macroscopic strains $\overline{\varepsilon} = 0, 65.0$, and $83.9\%$. Guided by the results of Fig. 4, the disk contains two defects located at the rubber/plates interfaces; their ratio $v^i/V$ of current volume $v^i$ to initial volume $V = 4/3\pi\Delta^3 \approx 4.19 \times 10^{-18}\text{m}^3$ is explicitly included to aid the visualization of their growth. Fig. 7(d) shows corresponding plots

of the normalized macroscopic stress $\overline{\sigma}/\mu$ and volume variation $v/V$ of the defects in terms of the applied strain $\overline{\varepsilon}$. The key difference in the behavior of this thicker test-piece compared to its thinner counterparts is that the defects at the interfaces do also start growing at around the critical strain ($\overline{\varepsilon} = 61.8\%$) predicted by the criterion (9), but this growth is dramatically slower. Consistent with this behavior, as shown by Fig. 7(d), the stress-strain relation of the disk with defects is also seen to be essentially identical to that of the disk without defects. This suggests that — as expected from the common experience of stretching a rubber band — internal defects in sufficiently thick rubber disks are inconsequential altogether for large ranges of applied macroscopic strains.

To summarize, the above results indicate that defects near the rubber/plates interfaces along the centerline of the rubber disk in poker-chip experiments always grow first. Also, if they were the only defects in the rubber, they would ultimately grow to large sizes, albeit very slowly for thick disks. Once defects at the center of the rubber are accounted for, the behavior of the interface defects changes radically, but only provided that the stress triaxiality (i.e., the ratio of hydrostatic to shear stresses) is sufficiently large at the center of the disk, namely, provided that the disk is sufficiently thin. In that case, the defect at the center is the only one that ends up growing to a very large size. The results further indicate that the growth of interface defects does not lead to significant softening of the overall mechanical response of the poker-chip test-piece, whereas the growth of the defect at the center does.

### *3.2.2 Defects across the midplane of the rubber disk and near the rubber/plates interfaces*

For sufficiently thin test-pieces, the attainability of the cavitation criterion (9) eventually propagates across the larger part of the rubber disk (see Figs. 2 and 3). In this subsection, we thus consider the explicit presence of defects across the rubber.

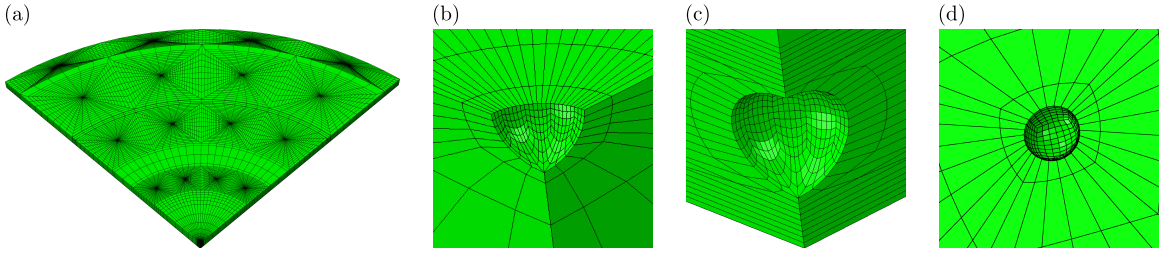


**Fig. 8** 3D FE model of the poker-chip test-piece with rubber disk thickness $H = 0.056$ cm containing 195 defects: (a) one eighth of the rubber disk illustrating the mesh refinement around the midplane defects, (b)–(c) details of the defects located in the midplane and the bottom rubber/plate interface of the disk along its centerline, and (d) detail of a defect located in the midplane of the disk away from its centerline.

*The FE model.* Because of the extremely small size of the defects (1 $\mu$m in radius), the discretization of the rubber disk explicitly containing defects is required to be in the form of a structured mesh. In practice, this requirement forces the spatial distribution of defects in the simulations to exhibit some level of periodicity thus preventing the consideration of a truly random distribution. For definiteness, based on the results from the preceding subsection and preliminary studies of a variety of distributions, we consider here that the defects are located within three planes: a plane adjacent (1 $\mu$m away) to the top rubber/plate interface, a plane adjacent (1 $\mu$m away) to the bottom rubber/plate interface, and the midplane of the rubber disk. Within each of these planes, 5 defects at radial distances $0, 0.25, 0.50, 0.75$, and $0.95$ cm from their center are placed at angular intervals of $\pi/8$ radians. This amounts to a total of 65 defects per plane, and thus a total of 195 defects in the entire rubber disk. Exploiting all inherent symmetries, the calculations can be performed over just one thirty-second of the rubber disk of interest. A mesh generator code is utilized to discretize such regions with eight-node hybrid linear elements with constant pressure (C3D8H in ABAQUS). Figure 8 illustrates a representative mesh for the case of the rubber disk with thickness $H = 0.056$ cm. Figure 8(a) shows one eighth of the entire disk for better visualization. Figures 8(b)–(d) show details of the mesh around the defects at various locations. Mesh sensitivity studies indicate that meshes of this sort with around 40,000 elements are refined enough to produce accurate results.

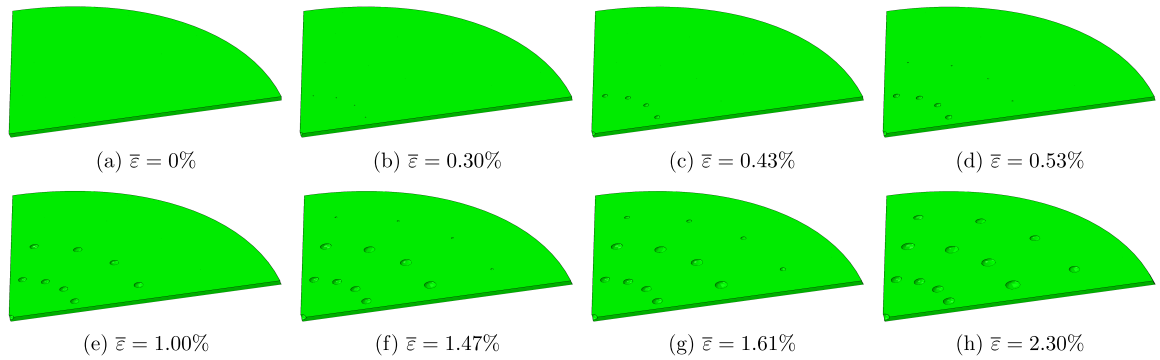


**Fig. 9** 3D FE simulation of the poker-chip experiment with rubber disk thickness $H = 0.056$ cm containing 195 defects throughout the entire disk. Parts (a) through (h) show snapshots of one eighth (for better visualization) of the rubber disk at eight values of the applied macroscopic strain $\overline{\varepsilon}$. The top surface in the snapshots corresponds to the midplane of the disk.

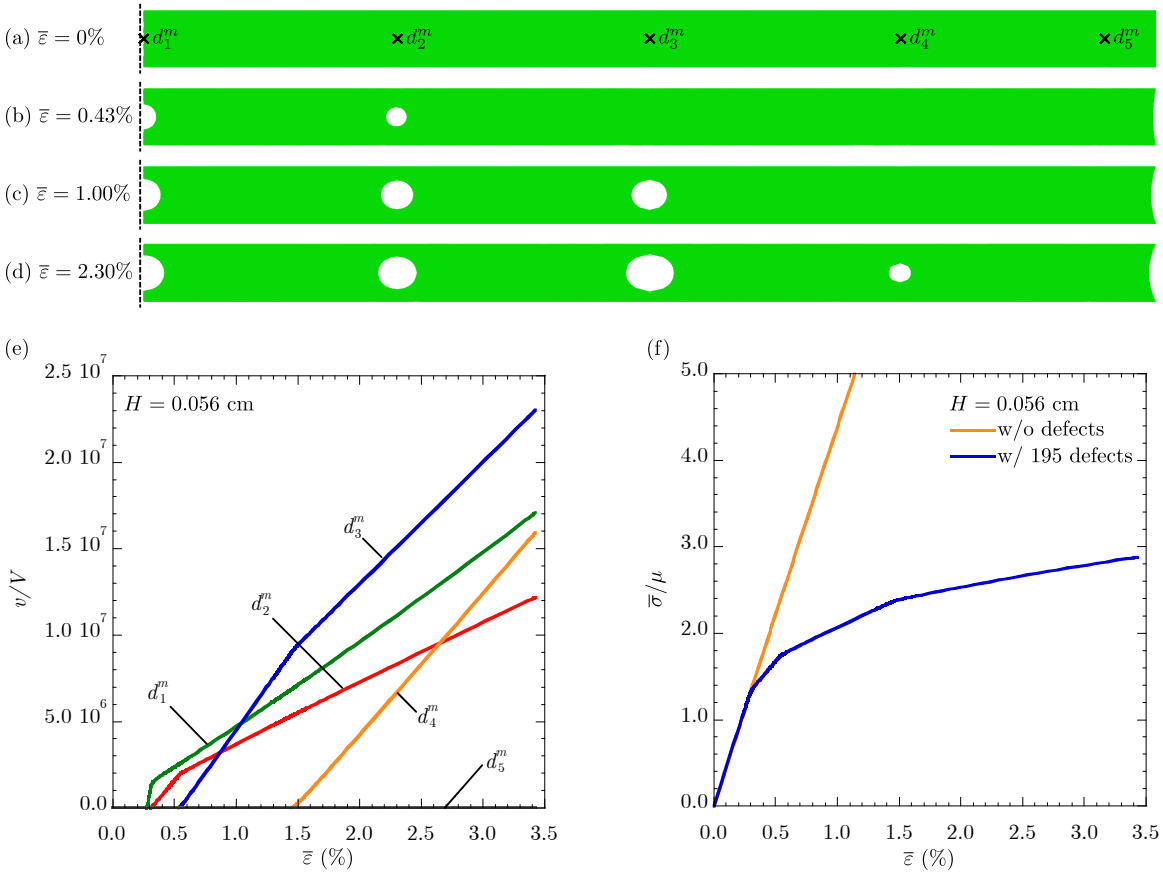


**Fig. 10** 3D FE simulation of the poker-chip experiment with rubber disk thickness $H = 0.056$ cm containing 195 defects throughout the entire disk. Parts (a) through (d) show a 2D radial perspective of half of the rubber disk at four values of the applied macroscopic strain $\overline{\varepsilon}$. Parts (e) and (f) show plots of the volume variation of the midplane defects — labeled $d_1^m$, $d_2^m$, $d_3^m$, $d_4^m$, and $d_5^m$ as indicated in part (a) — and the normalized macroscopic stress $\overline{\sigma}/\mu$ as functions of $\overline{\varepsilon}$.

*Results.* Figure 9 displays the deformed configurations of (one eighth of) the rubber disk with thickness $H = 0.056$ cm at the applied macroscopic strains $\overline{\varepsilon} = 0, 0.30, 0.43, 0.53, 1.00, 1.47, 1.61$, and $2.30\%$. The string of snapshots (a) through (h) show, from a 3D perspective, that the first defect to grow is the one

located in the center of the disk and that, upon further loading, adjacent midplane defects successively grow in a radial cascading sequence; as the exception, the defects closest to the lateral free boundary of the disk do not grow. This seemingly intricate behavior can be readily understood from an energetic standpoint. As already discussed within the context of Fig. 6, even though the cavitation criterion (9) is first satisfied at the rubber/plates interfaces slightly before than at the center of the disk (see Fig. 2), it is energetically more favorable for the defect at the center to accommodate all of the initial growth. As the macroscopic strain $\overline{\varepsilon}$ increases and satisfaction of the criterion (9) propagates radially outwards (see Fig. 2), it becomes energetically more favorable for the defects in the midplane of the disk adjacent to its center — and *not* those near the rubber/plates interfaces — to then accommodate most of the growth at the expense of the defect at the center. This radial cascading trend continues across the disk for increasing strains all the way up to reaching a narrow region containing the lateral boundary of the disk. There, the state of stress does not satisfy the criterion (9) and hence the underlying defects do not grow.

To aid the quantitative understanding of the above-described growth and interaction of defects and also their effect on the overall mechanical response of the poker-chip test-piece, Figs. 10(a)–(d) show a 2D radial perspective of half of the disk at various values of the applied macroscopic strain $\overline{\varepsilon}$. Additionally, Figs. 10(e) and (f) show corresponding plots of the volume variation $v/V$ of the midplane defects and of the normalized macroscopic stress $\overline{\sigma}/\mu$ as functions of $\overline{\varepsilon}$. For clarity of presentation, as marked in part (a) of the figure, the defects are labeled in a sequential manner as $d_i^m$ $(i = 1, 2, ..., 5)$ with $d_1^m$ denoting the defect at the center of the disk. Figures 10(a)–(e) distinctly illustrate the radial cascading nature of the growth of the midplane defects with increasing loading. The primary observation from Fig. 10(f) is that the growth of midplane defects entails a severe softening of the overall mechanical response of the rubber disk; the response of the perfect rubber disk without defects is plotted in the same figure for direct comparison. Again, since the rubber is assumed to remain elastic for arbitrarily large deformations, this softening is purely *geometrical* in nature.

Next, we turn to examine the response of the disk with moderate thickness $H = 0.190$ cm. Akin to Figs. 9–10, Figs. 11 and 12 show deformed configurations of such a disk from 3D and 2D perspectives at various values of the applied macroscopic strain $\overline{\varepsilon}$. They further show plots of the volume variation $v/V$ of the midplane defects and of the normalized macroscopic stress $\overline{\sigma}/\mu$ as functions of $\overline{\varepsilon}$. Again, as marked in Fig. 12(a), the midplane defects are labeled $d_i^m$ $(i = 1, 2, ..., 5)$ in an orderly manner with $d_1^m$ denoting the defect at the center of the disk.

In agreement with the simulations for the thinnest test-piece, Fig. 11 shows that the first defect to grow to finite size is the one located at the center of the rubber disk and that, upon further loading, the immediately adjacent row of defects in the midplane start to grow as well. Contrary to the simulations for the thinnest test-piece, however, no further radial cascading growth occurs upon continuing loading. Instead, the midplane defects adjacent to the center of the disk continue to accommodate most of the subsequent growth, at least for a large range of applied macroscopic strains $\overline{\varepsilon}$. Upon even further loading ($\overline{\varepsilon} > 5\%$), the defect at the center restarts to grow rapidly yet again. This sequence of events can be more clearly visualized from Figs. 12(a)–(d), and even more so from the plots shown in Fig. 12(e). Figure 12(f) also shows that such a growth of midplane defects results in a significant softening of the macroscopic stress-strain relation for the entire poker-chip test-piece.

In line with the physical motives behind the behavior of the thinnest rubber disk, the behavior of the rubber disk with the moderate thickness $H = 0.190$ cm can be understood from an energetic perspective. Indeed, while the cavitation criterion (9) is first satisfied at the rubber/plates interfaces along the centerline of the disk slightly before than at the center of the disk (see Fig. 3), it is energetically more favorable for the defect at the center to accommodate all of the growth, at least initially. As the macroscopic strain $\overline{\varepsilon}$ increases and satisfaction of the criterion (9) propagates radially outwards (see Fig. 3), it becomes energetically more favorable for the defects in the midplane of the disk just away from its center — and, again, *not* those near the rubber/plates interfaces — to accommodate most of the growth. As the macroscopic strain $\overline{\varepsilon}$ increases further, the criterion (9) continues to propagate radially outwards along the midplane but at a much slower rate than in the case of the thinnest disk (compare Fig. 3 with Fig. 2). Accordingly, in contrast to the behavior of the thinnest disk, it continues to be energetically more favorable for the midplane defects adjacent to the center of the disk to continue accommodating most of

the growth at the expense of the defect at the center and of those downstream in the direction of the lateral boundary, which remain small.

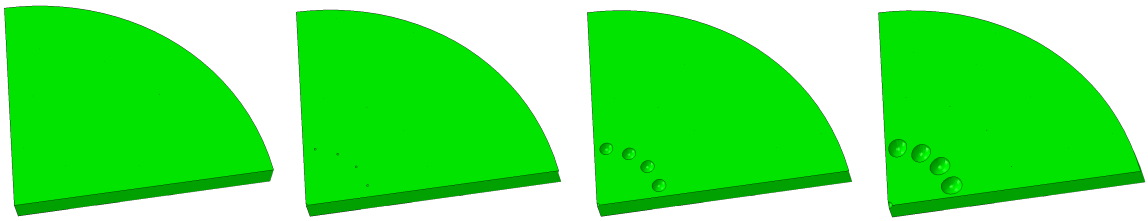

(a) $\overline{\varepsilon} = 0\%$ (b) $\overline{\varepsilon} = 3.35\%$ (c) $\overline{\varepsilon} = 4.03\%$ (d) $\overline{\varepsilon} = 5.40\%$

**Fig. 11** 3D FE simulation of the poker-chip experiment with rubber disk thickness $H = 0.190$ cm containing 195 defects throughout the entire disk. Parts (a) through (d) show snapshots of one eighth (for better visualization) of the rubber disk at four values of the applied macroscopic strain $\overline{\varepsilon}$. The top surface in the snapshots corresponds to the midplane of the disk.

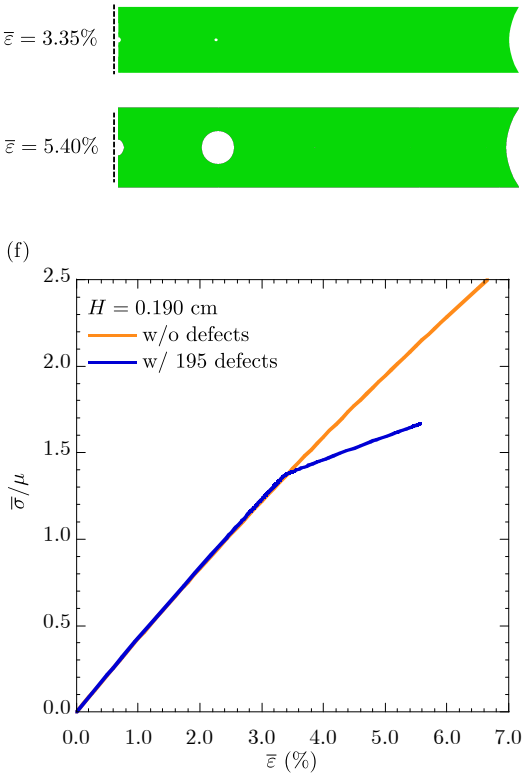


**Fig. 12** 3D FE simulation of the poker-chip experiment with rubber disk thickness $H = 0.190$ cm containing 195 defects throughout the entire disk. Parts (a) through (d) show a 2D radial perspective of half of the rubber disk at four values of the applied macroscopic strain $\overline{\varepsilon}$. Parts (e) and (f) show plots of the volume variation of the midplane defects — labeled $d_1^m$, $d_2^m$, $d_3^m$, $d_4^m$, and $d_5^m$ as indicated in part (a) — and the normalized macroscopic stress $\overline{\sigma}/\mu$ as functions of $\overline{\varepsilon}$.

Finally, as already discussed within the contexts of Figs. 4 and 7, the underlying defects in the thickest rubber disk with $H = 0.980$ cm do not grow, other than slowly in neighborhoods of the rubber/plates interfaces, to large sizes because the states of stress in most of the rubber disk do not reach the criterion (9). No additional results for this case are thus reported here.

In summary, the above results reveal that the defects that grow to large sizes in poker-chip test-pieces with thin rubber disks are those located in the midplane of the disks, and *not* those near the rubber/plates interfaces where the criterion (9) is satisfied first. This is because the midplane is farthest from the stiff rubber/plates interfaces and thus it is the location where the growth of defects is energetically least costly. More specifically, for thin enough rubber disks, growth of midplane defects starts at the center of the disk and then propagates radially outwards in a cascading sequence. All defects, except for those near the free lateral boundary, end up growing to comparable sizes. As the thickness of the rubber disk is increased, a similar cascading sequence occurs, but its propagation remains localized around the center of the disk. As the thickness of the rubber disk is increased even further, midplane defects do not grow at all. Instead, those near the rubber/plates interfaces do grow, but at such a slow rate that they remain largely inconsequential.

### 3.3 Elastic cavitation theory vs. experiments

We are now in a position to confront the foregoing theoretical results to the experimental observations and measurements of Gent and Lindley (1959). Figure 13 reproduces photographs of the midplane of three test-pieces, made up of the same natural rubber but different disk thicknesses $H = 0.061, 0.180$, and $0.370$ cm, cut open after being subjected to a macroscopic stress of $\overline{\sigma} = 2.74$ MPa; the shear modulus of the rubber is $\mu = 0.59$ MPa (labeled as vulcanizate D in Gent and Lindley, 1959). A key observation from this figure is that, irrespectively of the thickness of the rubber disk, cavities appear in the midplane of the disk and *not* elsewhere. Remarkably, this is in agreement with the simulations, even though the simulations assume that the rubber is Gaussian and that the defects can only grow elastically. This, of course, is not the case in the experiments. Indeed, the natural rubber utilized in the experiments is comprised of polymeric chains of finite length and thus its behavior is not Gaussian beyond moderately large deformations (typically in the order of 300%). Moreover, as plainly shown by the post-mortem snapshots in Fig. 13, the defects do grow inelastically by the irreversible creation of new surface.

(a) $H = 0.061$ cm (b) $H = 0.180$ cm (c) $H = 0.370$ cm

**Fig. 13** Midplane of poker-chip test-pieces, made up of the same natural rubber with initial shear modulus $\mu = 0.59$ MPa, cut open after being subjected to a macroscopic stress of $\overline{\sigma} = 2.74$ MPa. Parts (a), (b), and (c) correspond, respectively, to rubber disks with initial thicknesses $H = 0.061, 0.180$, and $0.370$ cm, as reported by Gent and Lindley (1959).

Another key observation from Fig. 13 is that for the thin disk with $H = 0.061$ cm, cavities appear pervasively over the entire midplane, with the exception of a narrow region around the lateral free boundary. For the moderately thick disk with $H = 0.180$ cm, on the other hand, the formed cavities remain localized around the center of the disk. Finally, for the thicker disk with $H = 0.370$ cm, only a single cavity appears in the center of the disk. Yet again, this behavior of localization towards the center of the disk with increasing rubber disk thickness is in agreement with the simulations. In spite of this agreement in location, the shape of the cavities in the experiments with disk thicknesses $H = 0.180$ cm and $H = 0.370$ cm are extremely anisotropic, which is not the case for the shapes of the cavities in the simulations. This is another manifestation of the fact that defects in actual rubber do grow inelastically via a fracture process.

While Gent and Lindley (1959) did not monitor the growth of the defects *in-situ* (other than in one of their specimens made up of transparent rubber, vulcanizate G), more recent poker-chip experiments have made used of X-ray computer tomography to access such information (Bayraktar et al., 2008). These experiments have shown that the cavities appear first in the center of the disk and subsequently downstream in the direction of the lateral boundary. This radial cascading sequence is also in agreement with the simulations.

In addition to post-mortem photographs of the test-pieces, Gent and Lindley reported various quantitative measurements as well. Figure 14(a) shows the macroscopic stress-strain relation for the poker-chip test-piece wherein the rubber has shear modulus $\mu = 0.59$ MPa and the thickness of the rubber disk is $H = 0.190$ cm. The dash line corresponds to the experiment, while the solid blue line corresponds to the simulation with 195 defects; the simulation for the perfect rubber disk without defects (solid orange line) is also plotted to aid the discussion. There is a clear disagreement between the experiment and the simulations. The disagreement occurs from the very beginning of the loading, prior to the occurrence of cavitation, when the local deformation within the rubber is small and thus its behavior can indeed be accurately modeled as Gaussian. This suggests that there might be some inconsistencies in the experimental measurements of the macroscopic strain, since the macroscopic stress is less likely to be inaccurate because the corresponding forces involved are fairly large, in the order of hundreds of newtons. This latter point is further supported by the fact that the critical macroscopic stress at which cavitation ensues in the simulation, $\overline{\sigma}_{cr} \approx 0.8$ MPa, is similar in value to that in the experiment, $\overline{\sigma}_{cr} \approx 1.1$ MPa. The same is not true for the values of the critical macroscopic strain. Another point of discrepancy distinctly shown by Fig. 14(a) is that the softening of the experimental stress-strain response appears significantly more pronounced than that of the simulation. While this is to be expected since material softening due to fracture — in addition to geometrical softening due to the growth of the defects — is present in the experiment but not in the simulation, experiments with more accurate measurements of the macroscopic strain and stress would be needed to corroborate this difference.

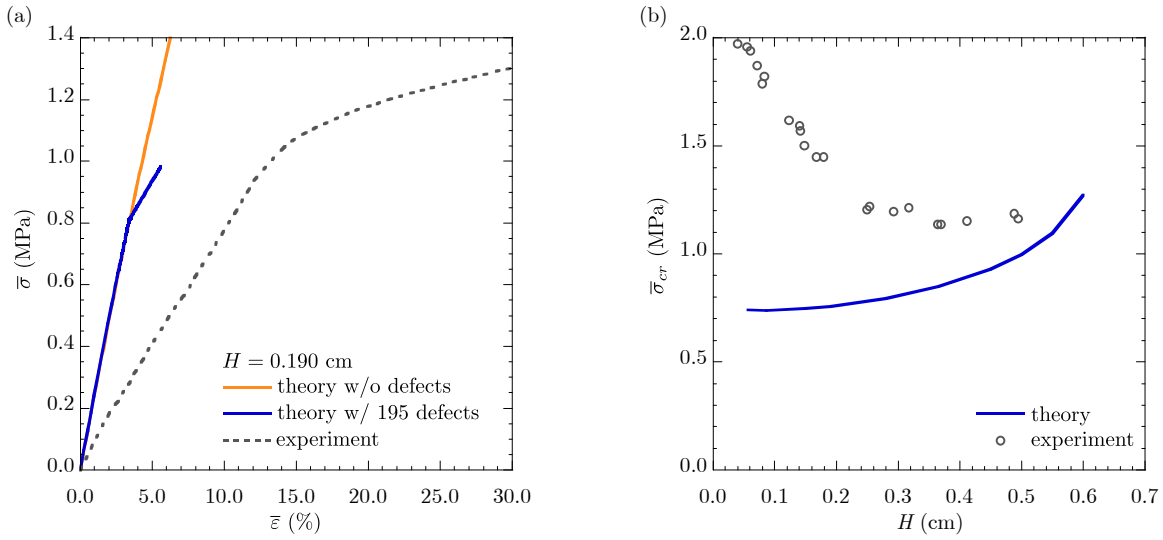


**Fig. 14** (a) Comparison of the experimental (dash line) and theoretical (solid lines) macroscopic stress-strain relation for the poker-chip test-piece with rubber disk thickness $H = 0.190$ cm. (b) Comparison of the experimental (circles) and theoretical (solid line) critical macroscopic stress, $\overline{\sigma}_{cr}$, at which cavitation ensues, plotted as a function of the thickness $H$ of the rubber disk. All of the results in parts (a) and (b) pertain to natural rubber with initial shear modulus $\mu = 0.59$ MPa, labeled as vulcanizate D in Gent and Lindley (1959).

To close, Fig. 14(b) shows plots of the the critical macroscopic stress, $\overline{\sigma}_{cr}$, at which cavitation ensues in terms of the thickness $H$ of the rubber disk also for the case of natural rubber with initial shear modulus $\mu = 0.59$ MPa. More precisely, the circles correspond to the values of the stress at which the stress-strain relation reaches its first local maximum in the experiments, presumably as a consequence of the finite growth of the underlying defects (Gent and Lindley, 1959). The solid line corresponds to the values of

the stress at which satisfaction of the general cavitation criterion (9) reaches the center of the rubber disk in the simulations; these values essentially indicate the point at which the macroscopic stress-strain relation starts to soften (because of the finite growth of the defects). To certain extent, the theoretical results predicted by the simulations are quantitatively similar to the experimental measurements (in the order of 1 MPa). Qualitatively, on the other hand, they are rather different. For test-pieces with rubber disk thickness in the range $H \in [0.056\,\text{cm}, 0.25\,\text{cm}]$, the critical stress at which cavitation ensues in the experiments decreases with increasing thickness. For test-pieces with $H \in [0.25\,\text{cm}, 0.5\,\text{cm}]$, the critical stress remains constant. And for those with $H > 0.5$ cm, cavitation does not occur. By contrast, the critical stress predicted by the simulations monotonically increases with increasing rubber disk thickness up to approximately $H = 0.6$ cm, beyond which cavitation does not occur. We note that the above-discussed qualitative difference between the experiments and the theory may be due in part to the fact that cavitation in experiments occurs well before the stress-strain relation reaches a local maximum. Experiments with a more direct detection of the onset of cavitation should be able to clarify this issue.

## 4 Comparison of the theory with the experiments of Gent and Park (1984)

Along the lines of the earlier work of Oberth and Bruenner (1965), Gent and Park (1984) studied the occurrence of cavitation near reinforcing particles in filled rubber via some ingenious experiments. They fabricated specimens comprised of a block of transparent rubber filled with two[2] small spherical particles placed in close proximity. They then subjected the entire block to quasistatic uniaxial tension in the direction of the alignment of the particles and monitored visually — through the transparent rubber — the occurrence of cavitation near the particles. The rubber utilized in the experiments was silicone rubber with an initial shear modulus of about 1 MPa. The spherical particles were comparatively rigid soda-lime glass beads of radius $R = 0.625$ mm. In order to obtain a good adhesion between the glass and the rubber, the surfaces of the beads were treated with a primer. Two cases with slightly different initial distances between the particles, denoted here as $D$, were reported. The values of these distances were not explicitly stated in their paper, but from the photographs provided they can be estimated as $D = 0.145$ and $0.190$ mm. Figure 15 shows a schematic of the geometry and deformation of the specimens with the various quantities of interest.

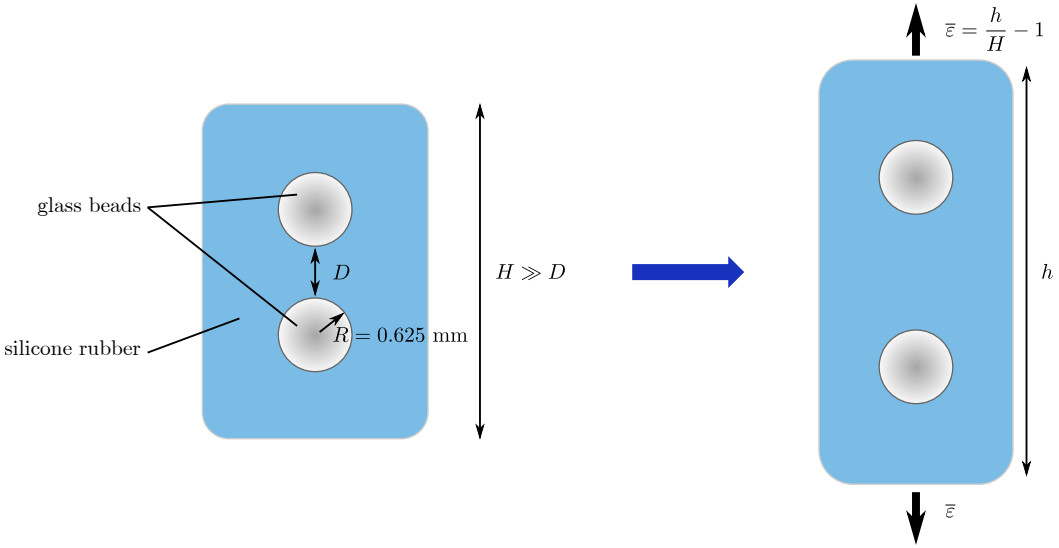


**Fig. 15** Schematic of the experimental setup of Gent and Park (1984). Two spherical glass beads of radius $R = 0.625$ mm were embedded in close proximity at an initial distance $D$ within the interior of a much larger block, with initial length $H$, of transparent rubber. The block was then subjected to uniaxial tension in the direction of the alignment of the particles. The macroscopic strain measure in the direction of the applied tensile load was defined as $\overline{\varepsilon} \doteq h/H - 1$.

[2] Gent and Park (1984) also studied specimens containing a single spherical filler particle. This simpler case is not considered here.

In this section, similar to the previous analysis of the poker-chip experiments, we report FE simulations of the experiments of Gent and Park (1984). We begin in subsection 4.1 by showing when and where the cavitation criterion (9) is satisfied for the two test-pieces with distances $D = 0.145$ and 0.190 mm between the particles, as a function of the macroscopic strain $\overline{\varepsilon}$. In subsection 4.2, we explicitly introduce defects — in the form of vacuous spherical cavities of $\Delta = 0.2$ $\mu$m radius — at the locations disclosed by the criterion into the FE models in order to examine how the "nucleated" cavities grow and interact upon further loading. We compare the simulations directly to the experiments in subsection 4.3.

### 4.1 Pointwise monitoring of the cavitation criterion

*The FE model.* For convenience and without loss of generality, the particles are considered to be located along the center of a circular cylindrical block with initial length $H = 160 \times R = 100$ mm and initial radius $H/2 = 50$ mm; this size is sufficiently large for the filler particles not to interact with the outer boundaries of the block. Since the shear modulus of soda-lime glass is in the order of 20 GPa, the particles are modeled as nonlinear elastic solids with the same form of stored-energy function (7) as the silicone rubber, but with a shear modulus four orders of magnitude larger. They are further assumed to be perfectly bonded to the rubber. The inherent geometric and constitutive symmetries of the problem allow to perform the calculations in just one half of a 2D-axisymmetric configuration of the test-piece of interest. The geometry of such regions is discretized with four-node hybrid linear elements with constant pressure (CAX4H in ABAQUS) in a way that smaller elements are placed around the particles. Figure 16 illustrates the mesh utilized for the case with particle distance $D = 0.145$ mm. It contains a total of about 30,000 elements, which proves refined enough to generate accurate results.

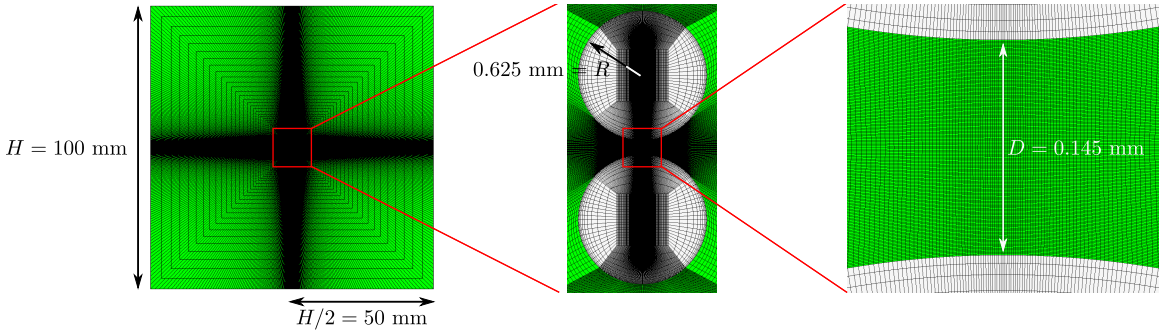


**Fig. 16** Axisymmetric FE model for the Gent-Park test-piece with two filler particles separated by a distance $D = 0.145$ mm.

*Results.* Figure 17 shows the deformed configurations of the region in between the particles of the simulated Gent-Park experiment with particle distance $D = 0.145$ mm at five different values of the macroscopic strain, $\overline{\varepsilon} = 0, 7.15, 9.10, 11.00$, and $20.00\%$. Material points at which the cavitation criterion (9) is satisfied are depicted in red; the points at which the hydrostatic criterion (10) is satisfied are also depicted to aid the discussion. The first points to reach the cavitation criterion are those located at the rubber/particles interfaces on the inner poles of the particles. The state of stress at those locations is almost purely hydrostatic, as can be deduced from the agreement between the predictions of the general and hydrostatic criteria shown by Fig. 17(b). At those locations, the value of hydrostatic stress is also the largest within the rubber. As the macroscopic strain increases, the satisfaction of the criterion propagates along the rubber/particles interfaces and also to the midpoint between the particles reaching it at the value $\overline{\varepsilon} = 11.00\%$; this is shown by Fig. 17(d). As the macroscopic strain increases even further, Fig. 17(e) shows that the region where the criterion is satisfied continues to grow radially outwards. In spite of the close distance between the particles, it is plain by glancing at the results based on the general and hydrostatic criteria that the effect of shear stresses is substantial.

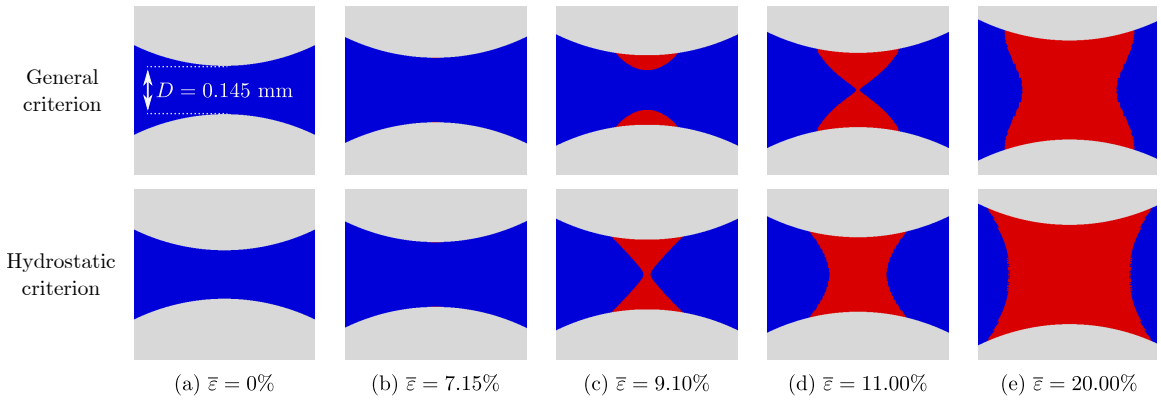


**Fig. 17** Axisymmetric FE simulation of the Gent-Park experiment with distance $D = 0.145$ mm between the particles. Parts (a) through (e) show the deformed configurations of the region between the particles at five values of the macroscopic strain $\overline{\varepsilon}$. The material points at which the general criterion (9) and the hydrostatic criterion (10) — included for comparison purposes — are progressively satisfied are depicted in red.

Figure 18 shows corresponding simulations of the Gent-Park experiment with the slightly larger particle distance $D = 0.190$ mm. The qualitative behavior, in the sense of when and where cavitation occurs, is seen to be essentially the same as that shown by Fig. 17. Quantitatively, however, the results are significantly different. Indeed, Fig. 18(b) shows that the onset of cavitation at the rubber/particles interfaces occurs at the sizably larger macroscopic strain $\overline{\varepsilon} = 9.60\%$ (compared to $\overline{\varepsilon} = 7.15\%$). Moreover, Fig. 18(d) shows that the onset of cavitation at the midpoint between the particles occurs also at the much larger value $\overline{\varepsilon} = 20\%$ (compared to $\overline{\varepsilon} = 11.00\%$). These results hence reveal that the state of stress between two nearby filler particles is extremely sensitive to the initial distance between them. In particular, small decreases in initial distance (e.g., here, 0.045 mm for particles of radius $R = 0.625$ mm) can result in significantly higher stress triaxialities, and thus an earlier onset of cavitation.

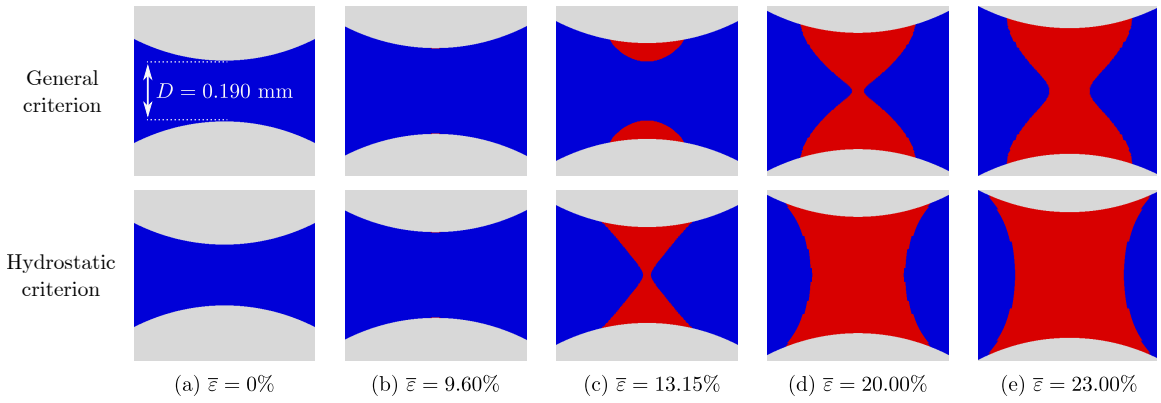


**Fig. 18** Axisymmetric FE simulation of the Gent-Park experiment with distance $D = 0.190$ mm between the particles. Parts (a) through (e) show the deformed configurations of the region between the particles at five values of the macroscopic strain $\overline{\varepsilon}$. The material points at which the general criterion (9) and the hydrostatic criterion (10) — included for comparison purposes — are progressively satisfied are depicted in red.

### 4.2 Full-field simulations accounting for the growth of the defects

Having determined the critical macroscopic loads and associated spatial locations at which defects in rubber may start to grow to finite sizes during Gent-Park experiments, we now turn to investigate the

extent to which they grow and how they interact with one another. To this end, again, we introduce defects explicitly in the FE models at the locations disclosed by the criterion (9) and monitor their growth. Here, much like in the analysis of the poker-chip experiments, defects are modeled as vacuous spherical cavities of initial radius $\Delta = 0.2$ $\mu$m; a variety of smaller defects of spherical and non-spherical shapes have been checked to lead essentially to the same results. Since the attainability of the cavitation criterion occurs first at the rubber/particles interfaces on the inner poles of the particles and then at the midpoint between the particles, we consider the explicit presence of defects sequentially at those locations.

*The FE model.* Introducing spherical defects at the poles of the particles and the midpoint between them does not perturb the geometric symmetry of the problem. Consequently, the relevant calculations can still be carried out over just one half of a 2D-axisymmetric configuration of the test-piece under investigation. Similar to the preceding analysis, four-node hybrid linear elements are utilized to discretize such regions with smaller elements placed around the defects. For illustration purposes, Fig. 19 depicts details of the mesh utilized for the case when three defects are introduced at the particle inner poles and midpoint between them for the test-piece with particle distance $D = 0.145$ mm. Figure 19(a) depicts the mesh near the defect at the inner pole of the top particle, while Fig. 19(b) depicts the mesh near the defect at the midpoint between the particles. Note that the defects at the poles are positioned 0.1 $\mu$m away from the rubber/particles interfaces in order to be able to mesh them appropriately. In all, the mesh contains a total of about 35,000 elements.

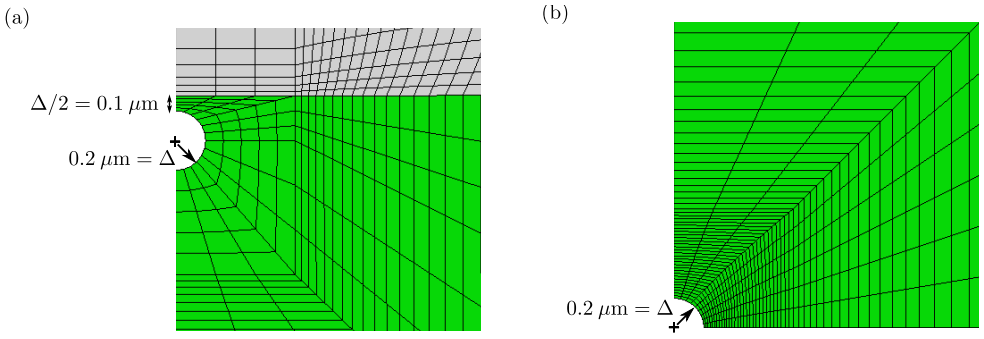


**Fig. 19** Details of the axisymmetric FE model for the Gent-Park test-piece with particle distance $D = 0.145$ mm containing three defects: two at the inner poles of the particles and one at the midpoint between the particles. Part (a) shows the defect at the interface between the rubber and the top particle, while part (b) shows the defect at the midpoint between the particles.

*Results.* Figure 20 shows simulations of the Gent-Park experiment with particle distance $D = 0.145$ mm containing two and three defects. Parts (a)–(d) and (i) correspond to results for the case when two defects are located at the rubber/particles interfaces, whereas parts (e)–(h) and (j) correspond to the case when there is an additional third defect located at the midpoint between the particles. In particular, Figs. 20(a)–(h) illustrate the deformed configurations of the region in between the particles at various values of the macroscopic strain $\overline{\varepsilon}$; the ratios $v^i/V$ and $v^m/V$ of current volumes $v^i$ and $v^m$ to initial volume $V = 4/3\pi\Delta^3 \approx 3.35 \times 10^{-20}$ m$^3$ of the defects at the $i$nterfaces and $m$idpoint are also displayed in these figures. Figs. 20(g) and (h) present corresponding plots of the volume variation of the defects as a function of $\overline{\varepsilon}$.

When the only defects that are accounted for are those at the rubber/particles interfaces on the inner poles of the particles, it is readily deduced pictorially from Figs. 20(a)–(d) and quantitatively from Fig. 20(i) that such defects start to grow suddenly to much larger sizes at around the critical strain $\overline{\varepsilon} = 7\%$ predicted by the criterion (9). They continue to grow upon further loading. By contrast, when an additional defect is also accounted for at the midpoint between the particles, Figs. 20(e)–(h) and (j) show a markedly different behavior. The sudden growth of the interfacial defects still ensues at around the critical strain

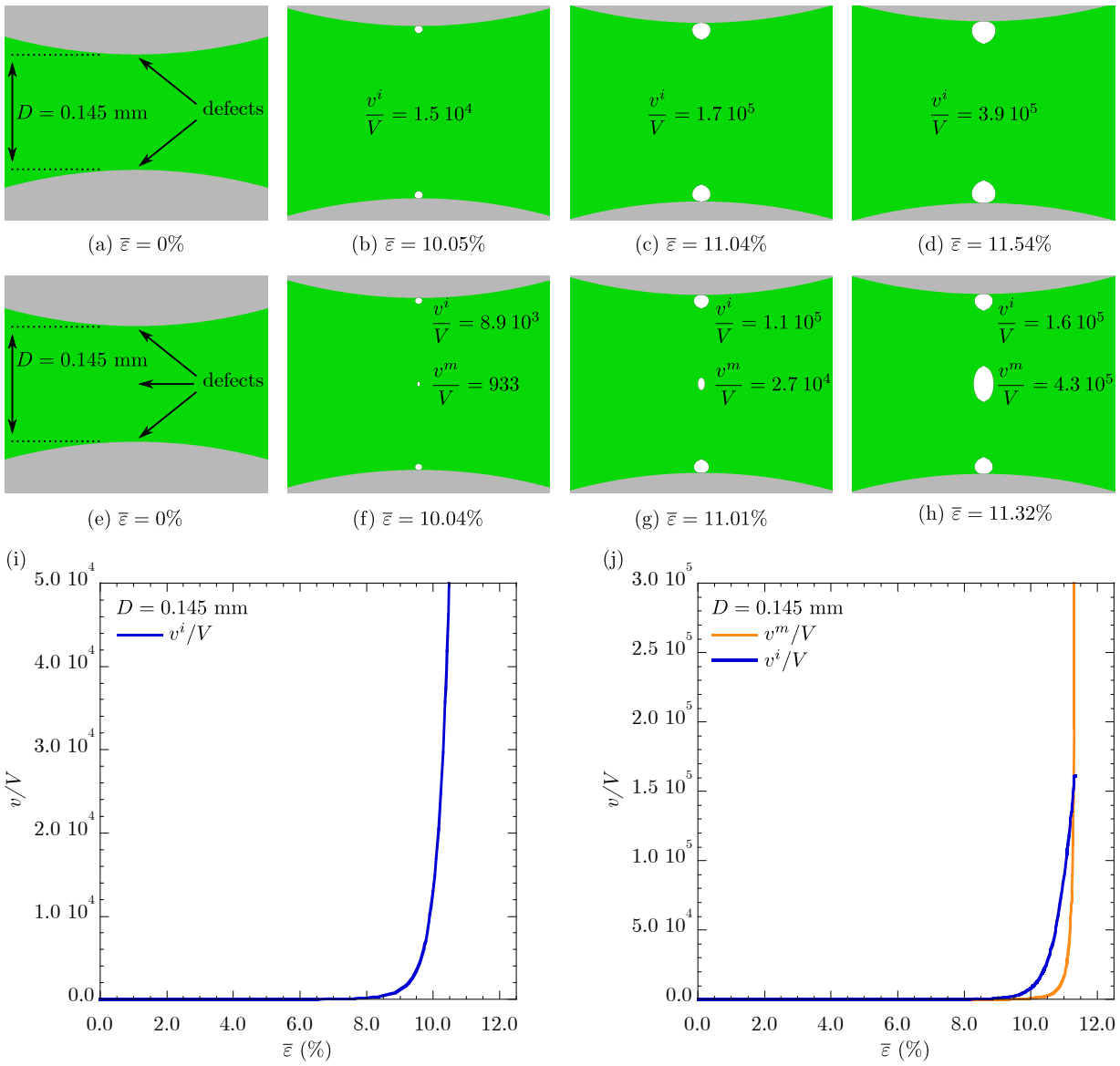


**Fig. 20** Axisymmetric FE simulations of the Gent-Park experiment with particle distance $D = 0.145$ mm containing two and three defects. Parts (a) through (d) and (i) show results when two defects are located at the rubber/particles interfaces on the inner poles of the particles. On the other hand, parts (e) through (h) and (j) show results when there is an additional third defect located at the midpoint between the particles. Figures (a)–(h) depict the deformed configurations of the region in between the particles at four values of the applied macroscopic strain $\overline{\varepsilon}$, while (i) and (j) show plots of the volume variation $v/V$ of the defects as a function of $\overline{\varepsilon}$.

$\overline{\varepsilon} = 7\%$. However, consistent with the prediction from the criterion (9), the midpoint defect starts to rapidly grow at around the macroscopic strain $\overline{\varepsilon} = 11\%$ and beyond in unison with a deceleration of the growth of the interfacial defects. These results are consistent with the fact that the growth of defects near the stiff rubber/particles interfaces is energetically more costly than at the midpoint between the particles, where it is in fact least costly. Accordingly, it is the defect at the midpoint the one that ends up accommodating the larger part of the growth.

The simulations of the Gent-Park experiment with the larger particle distance $D = 0.190$ mm containing analogous two and three defects are qualitatively the same as those shown by Fig. 20. The sole

difference is that the values of macroscopic strain at which the defects at the interfaces and subsequently at the midpoint grow are larger. For conciseness, no additional results for this case are thus included here.

In summary, the foregoing results reveal that the defects near the rubber/particles interfaces on the inner poles of the particles are the first to finitely grow during Gent-Park experiments. This is because, much like in the poker-chip results, the extreme mismatch in stiffness between the rubber and the filler particles leads to very large hydrostatic stresses on the inner poles of the particles and hence the cavitation criterion (9) is satisfied there first. As the loading progresses, the finite growth of a defect near the midpoint between the particles ensues at the expense of the interfacial defects whose growth comparatively stops. Again, much like in the poker-chip results, this is because the midpoint is farthest from the stiff rubber/particles interfaces and thus it is the location where the growth of defects is energetically least costly. As the loading progresses even further, the midpoint defect continues to accommodate most of the growth in detriment of the "nucleation" of more defects. Interestingly, this is in agreement with the behavior of defects in poker-chip test-pieces with thick rubber disks but in disagreement with that found in poker-chip test-pieces with thin rubber disks. The reason behind this disagreement is simply that defects in Gent-Park experiments are constrained to grow within the gap between two spheres instead of within the much more confined gap between two planes. The strong confinement in poker-chip test-pieces with thin rubber disks penalizes the localization of growth in a single defect and favors instead the growth of multiple defects.

### 4.3 Elastic cavitation theory vs. experiments

At this stage, we are equipped to compare the above theoretical results directly with the experiments of Gent and Park (1984). Figure 21 reproduces photographs of the Gent-Park experiment with particle distance $D = 0.145$ mm at three values of macroscopic strain, $\overline{\varepsilon} = 0, 17$ and 20%, and also after unloading. Figure 21(b) shows that cavities first appear near the inner poles of the particles at or before (their paper contains no evidence or statements as to when precisely the cavities first appear) the macroscopic strain $\overline{\varepsilon} = 17\%$. At the larger macroscopic strain $\overline{\varepsilon} = 20\%$, Fig. 21(c) shows that the cavities near the rubber/particles interfaces recede and a large cavity appears at the midpoint between the particles instead. Both of these events are in qualitative agreement with the simulations. Such an agreement is admittedly remarkable since, again, in addition to assuming that the rubber is Gaussian the simulations also assume that the defects can only grow elastically. Neither of these assumptions is in accord with the actual silicone rubber utilized in the experiment. For instance, Fig. 21(d) clearly shows that at least the midpoint defect in the experiment does grow inelastically via a fracture process.

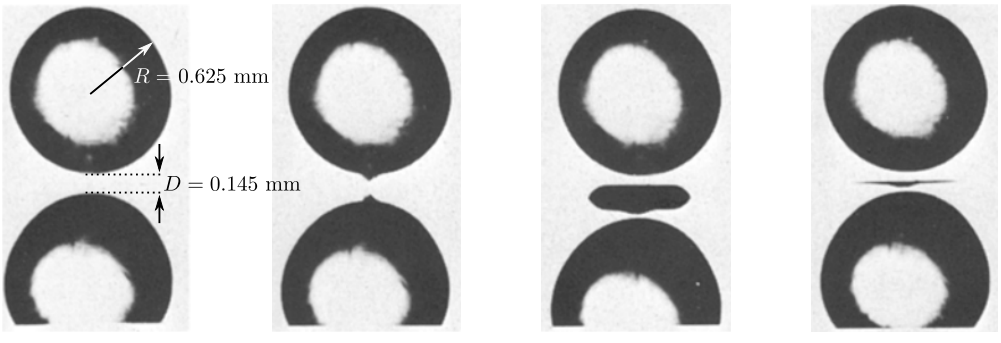


(a) $\overline{\varepsilon} = 0\%$ (b) $\overline{\varepsilon} = 17\%$ (c) $\overline{\varepsilon} = 20\%$ (d) After unloading

**Fig. 21** *In-situ* photographs of the Gent-Park experiment with initial distance $D = 0.145$ mm between the particles, of radius $R = 0.625$ mm, at macroscopic strains: (a) $\overline{\varepsilon} = 0$, (b) $\overline{\varepsilon} = 17\%$, and (c) $\overline{\varepsilon} = 20\%$. Part (d) shows a photograph of the specimen after unloading (Gent and Park, 1984).

In spite of the qualitative agreement pointed out above, there is a distinct quantitative discrepancy between the experiment shown in Fig. 21 and the corresponding simulation shown in Fig. 20. In the

simulation, cavities first appear near the inner poles of the particles at the macroscopic strain $\overline{\varepsilon} = 7\%$. At the larger macroscopic strain $\overline{\varepsilon} = 17\%$, the cavity at the midpoint has already enlarged to accommodate most of the total growth of all three defects. While Fig. 21 does not provide a conclusive macroscopic strain at which the cavities near the inner poles of the particles first appear in the experiment, it does show that the cavity at the midpoint appears only after the macroscopic strain $\overline{\varepsilon} = 17\%$. To better quantify this discrepancy, however, Gent-Park experiments with a continuous and more accurate spatiotemporal monitoring of the region between the particles would be needed.

Another important point of disagreement between the experiment shown in Fig. 21 and the corresponding simulation shown in Fig. 20 is the shape of the deformed cavity at the midpoint. In the simulation, the midpoint cavity exhibits a prolate shape aligned with the applied tensile force. In the experiment, on the other hand, the midpoint cavity exhibits an oblate shape aligned in the transverse direction to the applied tensile force. This is a clear manifestation that the midpoint defect in the experiment does grow inelastically by a fracture process, and not just elastically as assumed in the simulation.

## 5 Concluding remarks

The comparisons presented in Sections 3 and 4 have shown that theoretical results based on the premise that rubber is Gaussian and the further assumption that its inherent defects are vacuous and isotropically distributed are in good *qualitative* agreement with experiments in the sense of: (*i*) when and where cavitation first occurs as well as (*ii*) how cavities continue to grow and interact once they have been "nucleated". This remarkable agreement suggests that the sudden growth of defects and their ensuing behavior and interaction with other defects in real rubber is driven predominantly by the minimization of the elastic energy of the rubber. A direct practical implication of such a prominence of the elastic properties is that the *elastic* criterion (9) can be utilized effectively to gain quick insight into the possible occurrence of cavitation in real material systems comprising rubber.

The comparisons have further made it plain that the *quantitative* agreement between the theoretical results and the experiments is, as expected, poor. This is because the stiffening of rubber at large deformations (i.e., its departure from Gaussian behavior) and, more importantly, the fact that rubber ruptures at large but finite deformations (thus ceasing to be an elastic solid) are two features that need to be accounted for in the theoretical description of cavitation. While the microscopic mechanisms responsible for fracture in rubber are still unknown (in particular, it is yet unclear whether rubber fractures via changes in the conformation of the underlying polymeric chains or via the breaking of atomic bonds), it is expected that the rubber surrounding the defects at which cavitation occurs possess different mechanical properties than the rubber in the bulk. Accounting for the geometry and mechanical properties of such "damaged" regions of rubber in the theoretical description of cavitation appears also to be of the essence. In this context, it would be interesting to extend the elastic theory of Lopez-Pamies et al. (2011a) to account for all of the above-described three effects. The works of Williams and Schapery (1965) and Gent and Wang (1991) based on the ideas of Griffith (1921) may prove relevant in pursuing such an extension.

The results presented in Sections 3 and 4 have also revealed that there remains a need for more comprehensive and accurate sets of experimental data to advance the understating of the phenomenon of cavitation in rubber.

## Acknowledgements

This work was supported by the National Science Foundation through Grants DMS–1009503 and CMMI–1235352.

## References

1. ABAQUS Version 6.11 Documentation, Dassault Systemes Simulia Corp., Providence, RI, USA, 2011.
2. Ball, J.M. (1982) Discontinuous equilibrium solutions and cavitation in nonlinear elasticity. *Phil. Trans. R. Soc. A* 306: 557–611.

3. Bayraktar, E., Bessri, K., Bathias, C. (2008) Deformation behaviour of elastomeric matrix composites under static loading conditions. *Eng. Fract. Mech.* 75: 2695–2706.
4. Gent, A.N. (1991) Cavitation in rubber: A cautionary tale. *Rubb. Chem. Technol.* 63: G49–G53.
5. Gent, A.N., Lindley, P.B. (1959) Internal rupture of bonded rubber cylinders in tension. *Proc. R. Soc. Lond. A* 249: 195–205.
6. Gent, A.N., Park, B. (1984) Failure processes in elastomers at or near a rigid inclusion. *J. Mater. Sci.* 19: 1947–1956.
7. Gent, A.N., Wang, C. (1991) Fracture mechanics and cavitation in rubber-like solids. *J. Mater. Sci.* 26: 3392–3395.
8. Griffith, A.A. (1921) The phenomena of rupture and flow in solids. *Philosophical Transactions of the Royal Society of London* A221, 163–198.
9. Lopez-Pamies, O. (2009) Onset of cavitation in compressible, isotropic, hyperelastic solids. *Journal of Elasticity* 94: 115-145.
10. Lopez-Pamies, O., Idiart, M.I., Nakamura, T. (2011) Cavitation in elastomeric solids: I – A defect-growth theory. *J. Mech. Phys. Solids* 59: 1464–1487.
11. Lopez-Pamies, O., Nakamura, T., Idiart, M.I. (2011) Cavitation in elastomeric solids: II – Onset-of-cavitation surfaces for Neo-Hookean materials. *J. Mech. Phys. Solids* 59: 1488–1505.
12. Oberth, I.E., Bruenner, R.S. (1965) Tear phenomena around solid inclusions in castable elastomers. *Transactions of the Society of Rheology* 9: 165–185.
13. Stringfellow, R., Abeyaratne, R. (1989). Cavitation in an elastomer: Comparison of theory with experiment. *Materials Science and Engineering: A* 112, 127–131.
14. Williams, M.L., Schapery, R.A. (1965) Spherical flaw instability in hydrostatic tension. *Int. J. Fract. Mech.* 1: 64–72.